

Transport rates and momentum isotropization of gluon matter in ultrarelativistic heavy-ion collisions

Zhe Xu¹ * and Carsten Greiner¹

¹*Institut für Theoretische Physik, Johann Wolfgang Goethe-Universität Frankfurt,
Max-von-Laue-Str.1, D-60438 Frankfurt am Main, Germany*

(Dated: March 2007)

Abstract

To describe momentum isotropization of gluon matter produced in ultrarelativistic heavy-ion collisions, the transport rate of gluon drift and the transport collision rates of elastic ($gg \leftrightarrow gg$) as well as inelastic ($gg \leftrightarrow ggg$) perturbative quantum chromodynamics- (pQCD) scattering processes are introduced and calculated within the kinetic parton cascade Boltzmann approach of multiparton scatterings (BAMPS), which simulates the space-time evolution of partons. We define isotropization as the development of an anisotropic system as it reaches isotropy. The inverse of the introduced total transport rate gives the correct time scale of the momentum isotropization. The contributions of the various scattering processes to the momentum isotropization can be separated into the transport collision rates. In contrast to the transport cross section, the transport collision rate has an indirect but correctly implemented relationship with the collision-angle distribution. Based on the calculated transport collision rates from BAMPS for central Au+Au collisions at Relativistic Heavy Ion Collider energies, we show that pQCD $gg \leftrightarrow ggg$ bremsstrahlung processes isotropize the momentum five times more efficiently than elastic scatterings. The large efficiency of the bremsstrahlung stems mainly from its large momentum deflection. Due to kinematics, $2 \rightarrow N$ ($N > 2$) production processes allow more particles to become isotropic in momentum space and thus kinetically equilibrate more quickly than their back reactions or elastic scatterings. We also show that the relaxation time in the relaxation time approximation, which is often used, is strongly momentum dependent and thus cannot serve as a global quantity that describes kinetic equilibration.

PACS numbers: 25.75.-q, 12.38.Mh, 05.60.-k, 24.10.Lx

* E-mail: xu@th.physik.uni-frankfurt.de

I. INTRODUCTION

It is speculated that the quark gluon plasma (QGP) created in Au+Au collisions at the Relativistic Heavy Ion Collider (RHIC) is a strongly coupled liquid [1]. Because of strong coupling or rather strong interactions, the QGP fluid has a very small viscosity. However, questions regarding the source of the strong coupling and its needed strength to generate a quasi-ideal fluid remain unanswered. The necessary condition for the onset of perfect hydrodynamical expansion is the achievement of local kinetic equilibrium. Although the quarks and gluons produced at RHIC are far from thermal equilibrium, kinetic equilibration should occur on a short time scale so that the elliptic flow, v_2 , increases substantially [2, 3, 4]. In this article we assume that the strong coupling and thermalization are a consequence of frequent collisions among gluons on a semi-classical level. We recently developed a new on-shell parton cascade code, BAMPS (Boltzmann approach of multiparton scatterings) [5], which is a microscopical relativistic transport model that solves the Boltzmann equation for partons that are produced in ultrarelativistic heavy-ion collisions. The included interactions can be elastic $gg \leftrightarrow gg$ processes or inelastic $gg \leftrightarrow ggg$ pQCD bremsstrahlung processes. Although the total perturbative quantum chromodynamics- (pQCD) scattering cross section is only a few mb, it is enough to drive the system toward full thermal equilibrium [5] and also to generate sufficiently large elliptic flow v_2 [6]. Our goal is to understand the theoretical mechanism for the fast equilibration of gluons, which are observed numerically.

In kinetic theory there are two competing processes that affect kinetic equilibration. The first is when particles stream freely between two subsequent collisions. In an expanding system free streaming drives the system out of equilibrium. This is the case in a one-dimensional Bjorken expansion, which most likely occurs early on in ultrarelativistic heavy-ion collisions. The second one involves collisions that make the particle momentum kinetically isotropic and thermal. Here one has to take into account the distribution of collision angle because large-angle collisions should contribute more to momentum isotropization. We define isotropization as the development of an anisotropic system as it reaches isotropy. A *transport cross section* [7, 8] was introduced, either in the form

$$\sigma^{\text{tr}} = \int d\theta \frac{d\sigma}{d\theta} \sin^2 \theta \quad (1)$$

or

$$\sigma^{\text{tr}} = \int d\theta \frac{d\sigma}{d\theta} (1 - \cos \theta), \quad (2)$$

where θ denotes the collision angle as a pertinent quantity that measures the contributions of various collision processes to kinetic equilibration. Although kinetic equilibration is observed locally in the comoving frame of the expanding system, the transport cross section is usually calculated in the center-of-mass (c.m.) frame of individual colliding particles. The changes in momenta after the collision appears different in each respective frame. Therefore, the transport cross section may not be fully appropriate for characterizing kinetic equilibration.

A widely used, yet simpler, method to characterize kinetic equilibration is to calculate or estimate the relaxation time τ_{rel} [9, 10, 11, 12, 13, 14, 15]. In the relaxation time approximation the collision term is expressed by $(f_{\text{eq}} - f)/\tau_{\text{rel}}$, where τ_{rel} is assumed to be momentum independent and is then a global quantity that characterizes the kinetic equilibration time scale. However, the validity of the approximation must be verified.

In this article we derive a mathematical method of quantifying the contributions of various processes to the momentum isotropization. For this we define the *transport rate*, which is the momentum average of the particle density $f(x, p)$. The particle density is found within the parton cascade as a solution of the Boltzmann equation. Moreover, it will be shown that the inverse of the total transport rate gives the global time scale of momentum isotropization. In Sec. II we mention the operation of the employed parton cascade BAMPS and improvements made in it. The initial condition of gluons, as an input for the parton cascade, is discussed in Sec. III. We show results on thermal equilibration and momentum isotropization of gluons in Sec. IV for a central Au+Au collision at RHIC ($\sqrt{s} = 200$ GeV). The inclusion of quarks into the parton cascade is straightforward and the results will be presented in another article. In Sec. V we define the transport rates, which determine contributions of various processes to the momentum isotropization and derive their relations to the transport cross sections. We present in Sec. VI the numerical results on the transport rates. The transport rate of gluon drift is computed and compared with the one when obtained assuming Bjorken boost invariance. To show the importance of the bremsstrahlung processes in thermal equilibration, we carry out simulations with and without these processes for comparison. The quantitative difference in the momentum isotropization for both simulations is manifested by the ratio of the total transport rates. The ratio, which turns out to be approximately 6, is used to perform a third type of simulation in which only elastic

scatterings with artificially enlarged cross sections are included. Although such large cross sections are not physical, they verify our main finding: the total transport collision rate is the key quantity determining momentum isotropization. Despite the process type as long as the total transport collision rate is the same, the momentum isotropization is also the same. At the end of Sec. VI we demonstrate that the relaxation time approximation is not suitable for the quantification of the time scale for kinetic equilibration. A summary of our findings is given in Sec. VII. Detailed expressions for calculating the transport rates are derived in Appendix A.

II. BAMPS AND SETUP

The structure of the parton cascade BAMPS is based on the stochastic interpretation of the transition rate [5, 16, 17, 18]. This interpretation ensures that detailed balance is not violated, which is nontrivial when the geometrical concept of cross section is used [19], especially for multiple scatterings like $ggg \leftrightarrow gg$. BAMPS subdivides space into small cell units. In each of which we separately evaluate the transition probabilities of all possible gluon pairs and triplets to see if a particular scattering (or transition) occurs. The smaller the cells the more local transitions can be realized. However, the smaller cells contain fewer particles and thus have larger statistical fluctuations in their calculated transition rates. To achieve a high-enough number of pairs and triplets of gluons in a cell, we adopt a test particle technique, which amplifies the (pseudo)gluon density by a factor of N_{test} . Accordingly, the cross sections have to be reduced by the same factor to obtain the same physical mean free path [5]. In this article the transverse length of a cell is a constant of $\Delta x = \Delta y = 0.25$ fm and the longitudinal length Δz is half of that in [5], so for a cell of the center of the collision $\Delta z \approx 0.1t$, where t is the running time of the evolution of gluon matter. N_{test} is set to 280, which ensures that there are on average 15 test particles per cell.

The differential cross section for the elastic pQCD scatterings of gluons is given by

$$\frac{d\sigma^{gg \rightarrow gg}}{dq_{\perp}^2} = \frac{9\pi\alpha_s^2}{(q_{\perp}^2 + m_D^2)^2}. \quad (3)$$

Three-body gluonic interactions are described by the effective matrix element [13, 20, 21]

$$|\mathcal{M}_{gg \rightarrow ggg}|^2 = \frac{9g^4}{2} \frac{s^2}{(\mathbf{q}_{\perp}^2 + m_D^2)^2} \frac{12g^2\mathbf{q}_{\perp}^2}{\mathbf{k}_{\perp}^2 [(\mathbf{k}_{\perp} - \mathbf{q}_{\perp})^2 + m_D^2]} \Theta(k_{\perp}\Lambda_g - \cosh y) \quad (4)$$

where $g^2 = 4\pi\alpha_s$. α_s is set to 0.3 in contrast to the running coupling used in Ref. [5]. \mathbf{q}_\perp and \mathbf{k}_\perp denote the perpendicular component of the momentum transfer and of the radiated gluon momentum in the center-of-mass frame of the collision, respectively. y is the momentum rapidity of the radiated gluon in the center-of-mass frame, and Λ_g is the mean free path of a gluon.

We regularize the infrared divergences by introducing the Debye screening mass m_D

$$m_D^2 = 16\pi\alpha_s N_c \int \frac{d^3p}{(2\pi)^3} \frac{1}{p} f_g \quad (5)$$

($N_c = 3$), which is calculated locally using the current gluon density obtained from BAMPS. In general, the Debye screening mass should depend on the direction of the gluon propagator [22]. If the gluon distribution f_g significantly deviates from its isotropic shape, the Debye screening mass may even become negative, which leads to instabilities in certain modes of the soft gauge field [23, 24, 25, 26, 27, 28]. These instabilities and their proper inclusion are beyond the scope of the present article. We have simplified the problem by removing the directional dependence of the Debye screening mass.

The suppression of the radiation of soft gluons due to the Landau-Pomeranchuk-Migdal (LPM) effect [5, 13, 21] is included using the step function in Eq. (4). There the time of the emission, $\sim \frac{1}{k_\perp} \cosh y$, should be smaller than the time interval between two scatterings or equivalently the gluon mean free path Λ_g . This leads to a lower cutoff for k_\perp and a decrease in the total cross section or the transition probability.

Compared to the default setup in Ref. [5], further improvements have been made. To calculate the Debye screening mass m_D in a local region more accurately, we make use of the polar symmetry in central collisions and divide the transverse plane in each Δz -bin into rings: the first ring has a radial size of $0 < x_T < 1.5$ fm (x_T being the transverse radius), and the following rings have transverse radial widths of 1 fm. The rings are regarded as local regions in which the Debye screening mass is evaluated.

The local collision rates of all interaction channels, the sum of which is the inverse of the mean free path that models the LPM effect, were evaluated in Ref. [5] in individual cells. This leads to large fluctuations in the mean free path in cells with few (test) particles. To reduce these fluctuations we take the averaged value of the collision rates over all the cells within individual rings. In addition, transverse velocities of rings are taken into account to calculate the collision rates in the comoving frames.

Moreover, we assume that if the energy density, which is calculated locally in the comoving frame, sinks below $1 \text{ GeV}/\text{fm}^3$, particles in that region no longer interact, so they propagate freely. At this stage a hadronization procedure should be applied, which is planned as a future project.

We concentrate on the central region of the full reaction, which is defined as a cylinder with $0 < x_T < 1.5 \text{ fm}$ and $-0.2 < \eta < 0.2$ where η denotes the space-time rapidity $\eta = \frac{1}{2} \ln \frac{t+z}{t-z}$. The longitudinal extension of the cylinder is, thus, $\Delta z = 2t \tanh(0.2) \approx 0.4t$. The parameters for bounding the cylinder are found by balancing between having a small, local region and avoiding high statistical fluctuations. Results in this region are obtained by averaging over the various ensembles.

III. INITIAL CONDITIONS

Initial gluons are taken as an ensemble of minijets with transverse momentum greater than 1.4 GeV , which are produced via semihard nucleon-nucleon collisions [29]. Details of the distribution of the initial gluons in space and time can be found in Ref. [5]. Using Glauber-geometry and assuming independent binary nucleon-nucleon collisions, the gluon number is initially about 700 per momentum rapidity. These gluons take about 60% of the total given energy entered in a central Au+Au collision. The lower momentum cutoff is taken as a parameter to fit the experimentally measured final transverse energy at midrapidity (see Fig. 9).

For simplicity's sake one may assume that the two gold nuclei are extremely Lorentz contracted with zero width. Assuming that on-shell gluons are immediately formed (i.e., without any formation time) at the same time when the corresponding nucleon-nucleon collision occurs, all initial gluons are positioned at $z = 0 \text{ fm}$ at $t = 0 \text{ fm}/c$. Subsequent free streaming would immediately order the gluons with the momentum rapidity y to a spatial slice with the space-time rapidity η being equal to y . In the comoving frame of each spatial slice gluon momentum has only a transverse component and it has a highly anisotropic distribution.

At RHIC energy each of the colliding gold nuclei has a small but nonvanishing longitudinal extension of about 0.2 fm . Therefore, gluons are primarily produced at $z = 0 \text{ fm}$ (or $\eta = 0$) at $t \simeq 0.1 \text{ fm}/c$ when the two nuclei overlap fully. Note that $t = 0 \text{ fm}/c$ is when two nuclei

are just touching. In contrast to the simplified case mentioned above in reality there is a significant smearing in the gluonic $\eta - y$ correlation for times $t \leq 0.2$ fm/c. For instance, gluons with $y \neq 0$ will also appear in the central slice with $\eta = 0$ for a while. The rate of smearing disappearance is shown in Fig. 1, where the spectra of transverse and longitudinal gluon momenta are depicted during initial free streaming in absence of secondary collisions.

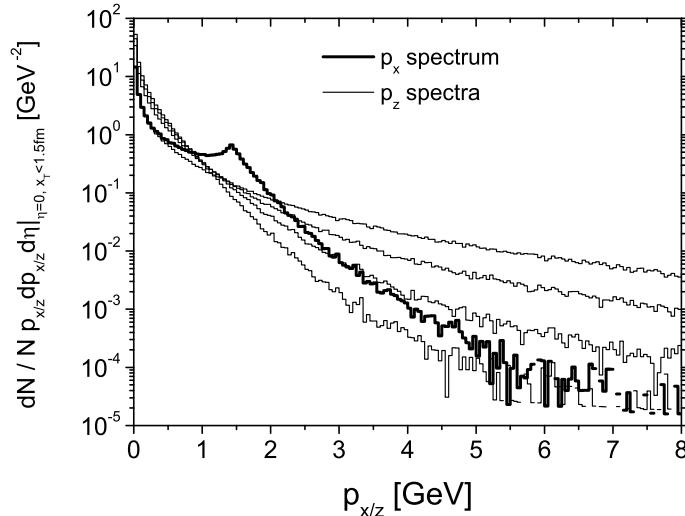


FIG. 1: Transverse and longitudinal gluonic momenta spectra during initial free streaming. The thick histogram is the distribution of $|p_x|$ at a time of 0.1 fm/c, whereas the thin histograms are the distributions of $|p_z|$ at times of 0.1, 0.2, 0.22, and 0.24 fm/c, respectively, from top to bottom. The results are obtained from the central region.

The spectra are obtained in the central region ($0 < x_T < 1.5$ fm and $-0.2 < \eta < 0.2$). We see that the $|p_z|$ spectrum changes quite drastically after 0.2 fm/c, the same point when two gold nuclei cease to overlap and the production of minijets is completed. The free streaming of high $|p_z|$ gluons away from the central region leads to strong, continuous suppression in the $|p_z|$ spectrum. Corresponding to this suppression, the changes in the $|p_x|$ spectrum at low transverse momentum are, however, tiny compared with their absolute values at low $|p_x|$. At high $|p_x|$ the change in time is negligible because there is no initial transverse expansion for large nuclei. Therefore, in Fig. 1 the $|p_x|$ spectrum is depicted only at $t = 0.1$ fm/c. We note that at large $|p_z|$ the suppression stops completely when all the particles with high p_z (or with high $y > \eta_b = 0.2$) have left the small, but finite, rapidity window $[-\eta_b : \eta_b]$. Then,

only particles with lower rapidity y remain in the central region. The time a gluon needs to leave the central region is, for instance, $\Delta t = t_0 \tanh \eta_b / (\tanh y - \tanh \eta_b)$ when the gluon is produced at $z_0 = 0$ fm at t_0 . We see that the larger the momentum rapidity y , the smaller Δt . For a gluon with $y = 1$ and $t_0 = 0.1$ fm/c it takes $\Delta t = 0.035$ fm/c to leave the central region.

Comparing the particle spectrum of $|p_z|$ with that of $|p_x|$, the momentum distribution is, strictly speaking, at no time isotropic during the initial free streaming. The characteristic hump in the $|p_x|$ spectrum at 1.4 GeV arises from the requirement that the transverse momentum of the original minijets should be greater than 1.4 GeV. Choosing other initial conditions like in HIJING [30, 31] or the color glass condensate [32] would change the shape of the initial momentum distribution. However, even though the momentum distribution might be isotropic during the continuing suppression of high $|p_z|$ gluons, the further suppression leads to a deviation in the momentum distribution away from isotropy within a very short time of ~ 0.1 fm/c. Therefore, we can conclude that free streaming leads to $\eta \approx y$ regardless of the initial $\eta - y$ correlation. The gluon momentum distribution after short-time free streaming is, in general, neither thermal nor isotropic.

In this article we introduce an additional *formation time* [5] for every minijet, $\Delta t_f = \cosh y \Delta \tau_f \approx \cosh y \cdot 1/p_T$, which models the prior off-shell propagation of the gluons to be freed in individual nucleon-nucleon collisions, where $\cosh y$ denotes the Lorentz factor. Within Δt_f we assume that the virtual gluon does not interact and, therefore, moves freely at the speed of light. Gluons with large $|p_z|$ have in turn a large Lorentz factor and, thus, a large formation time. Although most of these gluons are produced in the central region, they are far from the central region when they materialize as on-shell partons because of the assumed off-shell propagation. Because we count particles only if they are on-shell, i.e., interactive, the initial gluon momentum distribution at 0.2 fm/c differs from that shown in Fig. 1. However, it is practically identical to that at 0.24 fm/c, which is not isotropic. When the initial conditions are chosen accordingly and a simulation including the pQCD bremsstrahlung processes is performed, we obtain $dE_T/dy \approx 640$ GeV at midrapidity with a final time of 5 fm/c, at which the energy density of gluons decreases to the critical value of 1 GeV/fm³. Our dE_T/dy at $y = 0$ from the simulation is comparable with that found in experimental measurements at RHIC [33] (see Fig. 9).

IV. MOMENTUM ISOTROPIZATION AND KINETIC EQUILIBRATION

Kinetic equilibration is a process in which the particle momentum becomes isotropic and thermal, which has an exponential distribution. Momentum isotropization is part of kinetic equilibration and is reached before full kinetic equilibrium [25, 26, 27]. (Strictly speaking, full kinetic equilibrium can be achieved only for a static, nonexpanding system.) In this article we concentrate on the contribution of collision processes to momentum isotropization and kinetic equilibration of gluon matter in ultrarelativistic heavy-ion collisions.

As demonstrated in Sec. III, the initial free streaming (or the off-shell propagation) of gluons with high momentum rapidity y makes the momentum distribution anisotropic, even if it appears momentarily isotropic. Initially in the central region most gluons move in the transverse direction. Secondary collision processes gradually force them into the longitudinal direction, which gives a positive contribution to momentum isotropization. However, whenever a gluon switches to the longitudinal direction, its momentum rapidity grows and the gluon tends to drift out of the central region. This gives a negative contribution to momentum isotropization in the local region. Although gluons with the same (regardless of \pm sign) momentum rapidity drift from their neighboring slices into the central slice, this cannot completely compensate for the loss in the central region. The reason is that thermalization occurs earlier in the central slice than in the outwards regions corresponding to Bjorken's picture of boost-invariance in the space-time evolution of the parton system [34]. In the transverse direction, however, there is no transverse flow at the beginning of the expansion. Therefore, no net drift of gluons occurs in the transverse direction. The difference in the gluon drift in the longitudinal and transverse directions leads to a situation in which the net effect of the drift has a negative contribution to momentum isotropization and the stronger the momentum isotropization, the larger the negative contribution of the particle drift. At later times, when three-dimensional expansion takes place, there is also a net particle drift in the transverse direction and the negative contribution of the particle drift to momentum isotropization decreases.

In this section we first demonstrate momentum isotropization and kinetic equilibration of gluons in central Au+Au collisions at RHIC energy. The various contributions of collisions and drift to momentum isotropization will be analysed in detail in the next section. Figure 2 depicts the transverse and longitudinal gluon momenta distributions in the central region

at four different times throughout the evolution of gluon matter. The results are obtained

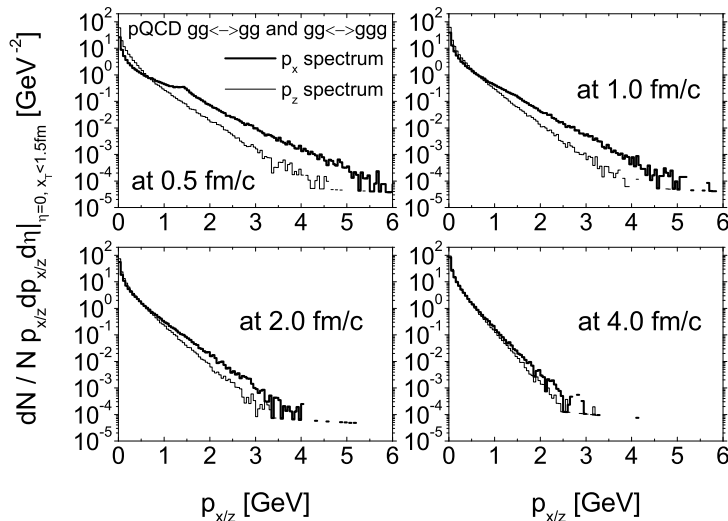


FIG. 2: Transverse (thick histograms) and longitudinal (thin histograms) gluon momentum spectra in the central region at various times throughout the evolution of gluon matter. Results are obtained from the simulation when both elastic and inelastic pQCD-scattering processes are included.

when both elastic and inelastic pQCD-based scattering processes are included. We first see that the momentum distribution continuously isotropizes and thermalizes over time. Due to the expansion full thermal equilibrium cannot be achieved if the collision rate is finite. A certain mismatch in p_z and p_x must exist due to the counteraction between the expansion and the collisions.

Second, Fig. 2 shows that there is an exponential distribution before the system becomes isotropic. It is almost impossible to distinguish the gluon momentum isotropy time scale from the thermal time scale. It seems that when collisions drive the particle momentum close to isotropy, the momentum distribution is already practically thermalized. In general, momentum isotropization happens on a shorter time scale than kinetic equilibration. The difference in the time scales of both dynamical processes depends on the initial condition for gluons.

Kinetic equilibration for the softer gluons is completed earlier than that for the harder gluons. This is obvious for elastic $gg \leftrightarrow gg$ scattering processes because the momentum transfer in collisions is typically the Debye screening mass. Therefore, the hard gluons cannot be deflected as strongly as the soft gluons. However, in the inelastic pQCD $gg \leftrightarrow$

ggg collisions, which we will prove are the dominant processes in kinetic equilibration, the difference in the momentum degradation for soft and hard gluons is miniscule due to the production or absorption of an additional gluon. Averaging the various kinetic equilibrium times for soft and hard gluons the momentum distribution becomes *isotropic and thermal* at $1 - 2 \text{ fm}/c$. Furthermore, we clearly see that the distributions become steeper with time, which indicates the ongoing cooling of the system related to quasi-hydrodynamical behavior due to the subsequent work done by the expanding system.

To understand the role of the inelastic pQCD $gg \leftrightarrow ggg$ processes in kinetic equilibration, we also carry out calculations in which gluons interact only via elastic scatterings. The initial conditions are the same as those when inelastic collisions are included. The results are shown in Fig. 3, which has the same structure as Fig. 2. The difference in the results depicted

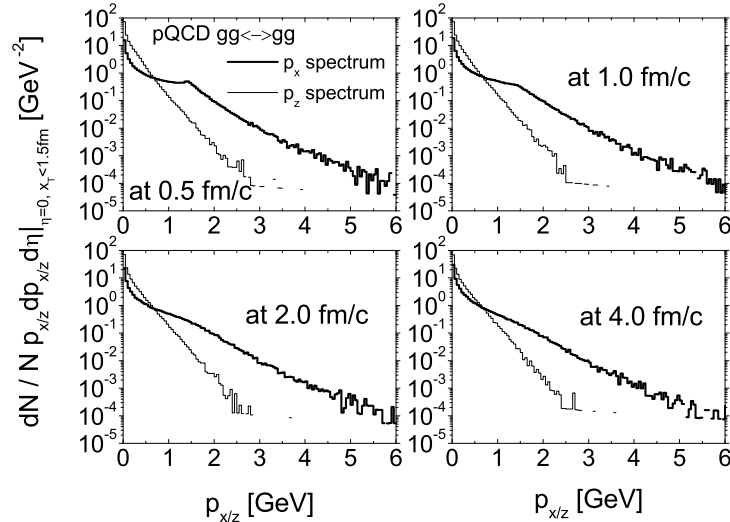


FIG. 3: Transverse (thick histograms) and longitudinal (thin histograms) gluon momentum spectra in the central region at various times throughout the evolution of gluon matter. Results are obtained using elastic only pQCD-scattering processes.

in both figures can be immediately seen. The spectra in Fig. 3 only show a small change throughout the entire evolution of the system and are still highly anisotropic and are not thermalized as late as $4 \text{ fm}/c$. The evolution resembles that of free streaming.

The kinetic equilibration time strongly depends on whether the pQCD bremsstrahlung processes and their back reactions are taken into account. The pQCD bremsstrahlung processes and their back reactions isotropize the momentum more efficiently than elastic

collisions and, thus, play an essential role in early thermalization of gluons in heavy-ion collisions at RHIC. As seen in Fig. 4, the pQCD cross section of $gg \rightarrow ggg$ processes, including LPM suppression (dashed curve), is *smaller* than that of elastic scatterings (solid curve) and much smaller than the cross section obtained in the simulation with elastic-only scattering processes (dotted curve). Although particle production in inelastic processes can

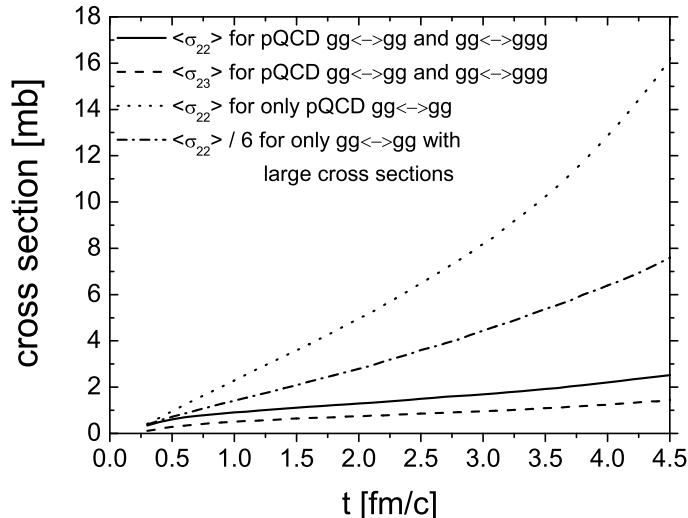


FIG. 4: Time evolution of pQCD cross sections. The solid and dashed curve show the pQCD cross section for $gg \rightarrow gg$ and $gg \rightarrow ggg$ collisions, respectively, when both elastic and inelastic scattering processes are considered. The dotted curve gives the cross section of $gg \rightarrow gg$ collisions in the simulation, including elastic-only pQCD scattering processes, whereas the dash-dotted curve indicates the cross section (*divided by a factor of 6*) of $gg \rightarrow gg$ collisions when elastic-only scattering processes with artificially large cross sections are included.

enhance the number of collision centers and, thus, effectively shorten the mean free path of particles, chemical equilibration will balance the production by the annihilation of particles to avoid oversaturation. The fact that the cross section of the pQCD bremsstrahlung process is small, but its kinetic equilibration efficiency is large, demonstrates that cross sections or collision rates are not the correct quantities to describe the contributions of various processes to kinetic equilibration. The collision-angle distribution must be at least taken into account. Defining the correct quantity is one of the main purposes for this article.

In Fig. 4 the large difference in the total cross sections of elastic scatterings for various

simulations is shown. Because

$$\langle\sigma_{gg\rightarrow gg}\rangle \sim \frac{1}{m_D^2 \langle 1 + 4m_D^2/s \rangle}, \quad (6)$$

the difference in the cross sections arises from the difference in the development of the Debye screening mass m_D in the various simulations. m_D is calculated dynamically according to (5) and, thus, is roughly proportional to $\sqrt{n/\langle p \rangle} = n/\sqrt{\epsilon}$, where n and ϵ are the number and energy density of gluons, respectively.

We consider two extreme cases of expansion with initial conditions that possess the longitudinal boost invariance. One case is free streaming, for which n as well as ϵ decrease as τ^{-1} , where $\tau = \sqrt{t^2 - z^2}$ is the proper time. Thus, m_D decreases as $\tau^{-1/2}$. In the other case of a one-dimensional ideal hydrodynamical expansion, n decreases as τ^{-1} , whereas ϵ decreases as $\tau^{-4/3}$. Therefore, m_D decreases as $\tau^{-1/3}$. In a viscous hydrodynamical expansion the decrease of m_D over time falls between the two cases. The time dependence of the Debye screening mass in a real expansion starting out of thermal equilibrium and undergoing thermalization is more complicated. Whereas kinetic equilibration drives the density distribution of gluons to its thermalized shape, which affects the calculation of m_D (5), chemical equilibration, which is not taken into account above, will enhance or reduce the gluon number, which in turn enhances or reduces m_D .

Figure 5 shows the time evolution of the Debye screening mass in various simulations. The results are obtained in the central region where $t \approx \tau$. All the curves in Fig. 5 decrease with time. Similar calculations for the Debye screening mass have been done in Refs. [35, 36] employing the parton cascade VNI/BMS. From Fig. 5 we see that the evolution depends on the simulation type: in the simulation including both elastic and inelastic pQCD scatterings (solid curve) m_D decreases slower than $t^{-1/3}$ due to gluon production in the course of chemical equilibration; in the simulation with elastic-only pQCD collisions the decrease of m_D (dotted curve) is slightly stronger than $t^{-1/2}$, which indicates again that the expansion of gluons in this simulation resembles that of free streaming; the third simulation includes elastic-only scatterings with artificially large cross sections and shows the same kinetic equilibration as that in the simulation including both elastic and inelastic pQCD collisions (see Fig. 6). The Debye screening mass in this simulation (dash-dotted curve) decreases between $t^{-1/2}$ and $t^{-1/3}$.

Returning to the kinetic equilibration analysis, the gluon kinetic equilibration time can

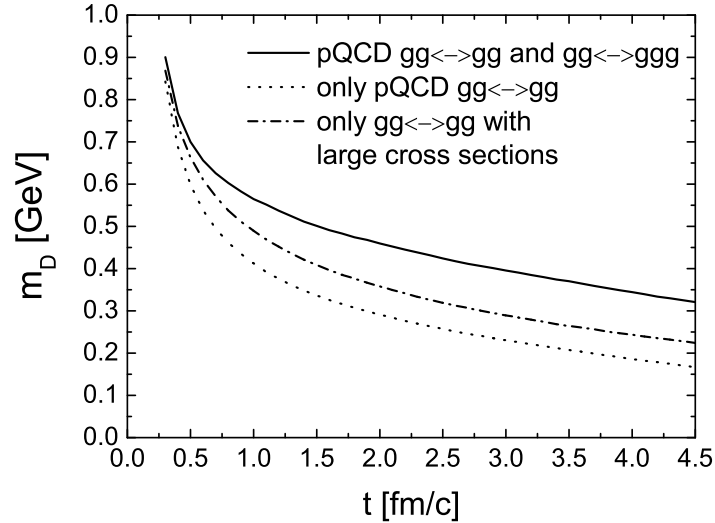


FIG. 5: Time evolution of the Debye screening mass. Results are obtained from the simulation with both pQCD elastic and inelastic collisions (solid curve), with elastic-only pQCD collisions (dotted curve), and with elastic-only collisions using large cross sections (dash-dotted curve).

in principle be determined quantitatively by studying the entropy production. Because the entropy can be hardly extracted from any microscopic cascade, we concentrate on momentum isotropization of gluons. Choosing minijets production as the initial condition, momentum isotropization and kinetic equilibration time scales are almost identical (as seen in Fig. 2).

To quantify momentum isotropization we have to choose an appropriate momentum-distribution moment Q . For instance, $Q := \langle p_z^2/E^2 \rangle$ is used to describe momentum isotropization. Later we briefly discuss the consequences of $Q = \langle |p_z|/E \rangle$, to see how sensitive the results are to different descriptions of momentum isotropization. In Fig. 6 momentum isotropization with $Q = \langle p_z^2/E^2 \rangle$ is depicted. The average is taken over all gluons in the central region. In Fig. 6 we see that Q relaxes its equilibrium value of $1/3$ when the inelastic processes are included, whereas it still deviates from its equilibrium value at the time 4.5 fm/c when only elastic pQCD scatterings are considered. These results agree with the momentum spectra time evolution shown in Figs. 2 and 3. The dash-dotted curve in Fig. 6 depicts the momentum isotropization considering elastic-only collisions with artificially large cross sections and is almost the same as the solid curve, which implies they have basically the same kinetic equilibration. The third simulation is detailed in Sec. VI.

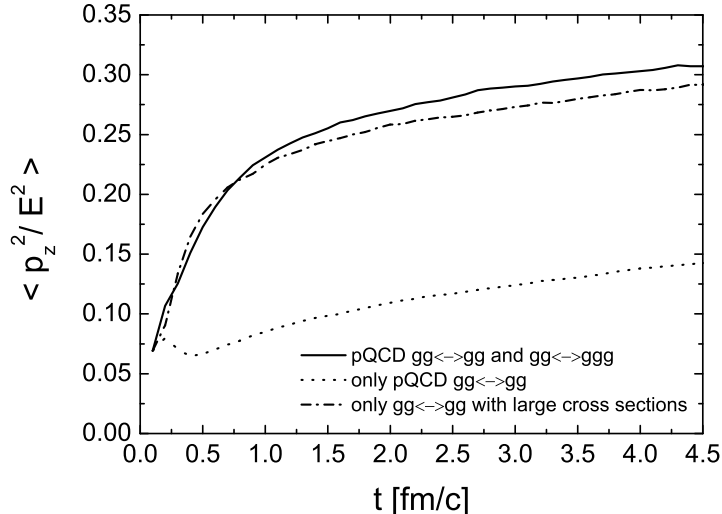


FIG. 6: Momentum isotropization. Results are obtained from the simulation with both elastic and inelastic pQCD-scattering processes (solid curve), with elastic-only pQCD-scattering processes (dotted curve) and with elastic-only scattering processes using artificially large cross sections (dash-dotted curve).

The momentum isotropization fit is found using the relaxation formula

$$F(t) = \frac{1}{3} + \left[Q(t_0) - \frac{1}{3} \right] \exp \left[-\frac{t - t_0}{\theta_{\text{rel}}(t_0)} \right]. \quad (7)$$

$F(t)$ is equal to $Q(t)$ only at $t = t_0$. For every fixed t_0 the relaxation time θ_{rel} is constant with respect to t . Using $\theta_{\text{rel}} = 0.9$ fm/c at $t_0 = 0.3$ fm/c up to 1.0 fm/c and $\theta_{\text{rel}} = 2.4$ fm/c at $t_0 = 1.2$ fm/c for the rest, $F(t)$ is a perfect fit for the solid curve in Fig. 6. An isotropy is achieved at about 1.0 fm/c in the simulation that includes both elastic and inelastic pQCD-scattering processes. This time scale is consistent with that extracted from the momentum distribution (see Fig. 2). Within our parton cascade description early thermalization occurs at roughly 1 fm/c for the initially nonequilibrated gluon matter at RHIC.

The relaxation time θ_{rel} is generally time dependent. Because a local fit requires that the time derivatives of $F(t)$ and $Q(t)$ are equal at $t = t_0$, which leads to

$$\dot{Q}(t) \Big|_{t=t_0} = \dot{F}(t) \Big|_{t=t_0} = -(Q(t_0) - Q_{\text{eq}}) \frac{1}{\theta_{\text{rel}}(t_0)}, \quad (8)$$

where $Q_{\text{eq}} = 1/3$, θ_{rel} can be calculated as [changing t_0 to t in Eq. (8)]

$$\frac{\dot{Q}(t)}{Q_{\text{eq}} - Q(t)} = \frac{1}{\theta_{\text{rel}}(t)}. \quad (9)$$

Equation (9) expresses the relaxation rate of momentum isotropization $1/\theta_{\text{rel}}$ as a function of time, which will be separated analytically into terms corresponding to the particle drift and the various scattering processes. We will derive the so-called *transport rates*, which *precisely* quantify the contributions of various processes to momentum isotropization.

V. TRANSPORT RATE

To introduce Q at a certain space point $\vec{\xi}$ one has to consider its comoving frame. For the coordinate x and the momentum four-vector p in the $\vec{\xi}$'s comoving frame, Q is defined by

$$Q(t) := \left\langle \frac{p_z^2}{E^2} \right\rangle \Big|_{\vec{x}=0} = \frac{1}{n} \int \frac{d^3p}{(2\pi)^3} \frac{p_z^2}{E^2} f(\vec{x}, t, p) \Big|_{\vec{x}=0}, \quad (10)$$

where the local number density is

$$n(t) = \int \frac{d^3p}{(2\pi)^3} f(\vec{x}, t, p) \Big|_{\vec{x}=0}. \quad (11)$$

In practice Q is evaluated within a volume element, which is small compared to the volume of the expanding system but is large enough so that it still contains a large number of particles. For the calculations shown in Fig. 6 we used the central region bounded by $x_T < r_b = 1.5$ fm and $|\eta| < \eta_b = 0.2$. Correspondingly (10) and (11) must also be adjusted and detailed expressions are derived explicitly in Appendix A. As a simplification we now consider the limit $r_b \rightarrow 0$ and $\eta_b \rightarrow 0$ where definitions (10) and (11) can be used.

Taking the time derivative of $Q(t)$ yields

$$\dot{Q}(t) = \frac{1}{n} \int \frac{d^3p}{(2\pi)^3} \frac{p_z^2}{E^2} \frac{\partial f}{\partial t} \Big|_{\vec{x}=0} - Q(t) \frac{1}{n} \int \frac{d^3p}{(2\pi)^3} \frac{\partial f}{\partial t} \Big|_{\vec{x}=0}. \quad (12)$$

We replace $\partial f/\partial t$ in Eq. (12) by

$$\frac{\partial f}{\partial t} = -\frac{\vec{p}}{E} \cdot \vec{\nabla} f + C_{22} + C_{23} + C_{32} \quad (13)$$

from the Boltzmann equation, where $-\frac{\vec{p}}{E} \cdot \vec{\nabla} f$ corresponds to particle drift and C_{22} , C_{23} , and C_{32} denote the collision terms corresponding to $gg \rightarrow gg$, $gg \rightarrow ggg$, and $ggg \rightarrow gg$, respectively. It is obvious that the contribution of the various processes to $\dot{Q}(t)$ is additive.

We rewrite Eq. (12)

$$\dot{Q}(t) = W_{\text{drift}}(t) + W_{22}(t) + W_{23}(t) + W_{32}(t), \quad (14)$$

where W_{drift} , W_{22} , W_{23} , and W_{32} correspond to particle drift, $gg \rightarrow gg$, $gg \rightarrow ggg$, and $ggg \rightarrow gg$ collision processes, respectively. According to Eq. (9) we obtain

$$\frac{1}{\theta_{\text{rel}}(t)} = R_{\text{drift}}^{\text{tr}}(t) + R_{22}^{\text{tr}}(t) + R_{23}^{\text{tr}}(t) + R_{32}^{\text{tr}}(t), \quad (15)$$

where we define

$$R_i^{\text{tr}}(t) := \frac{W_i(t)}{Q_{\text{eq}} - Q(t)} \quad (16)$$

for $i = \text{drift}, 22, 23, \text{ and } 32$. One sees that the relaxation rate of momentum isotropization $1/\theta_{\text{rel}}$ is separated into additive parts corresponding to the particle drift and the various collision processes. $R_{\text{drift}}^{\text{tr}}$ is called the *transport rate of particle drift*, whereas R_{22}^{tr} , R_{23}^{tr} , and R_{32}^{tr} stand for the *transport collision rates* of their respective interactions. Extending this to more than three-body processes is straightforward because the collision term is additive. We note that R_i^{tr} (shown below) depends on the definition of Q . When one changes Q from $Q = \langle p_z^2/E^2 \rangle$ to $Q = \langle |p_z|/E \rangle$, the form of R_i^{tr} changes accordingly.

A. $R_{\text{drift}}^{\text{tr}}$

Except for static systems the drift term in the Boltzmann equation (13) generally contributes to $\dot{Q}(t)$. W_{drift} is given by

$$W_{\text{drift}}(t) = \frac{1}{n} \int \frac{d^3p}{(2\pi)^3} \frac{\vec{p}}{E} \cdot \vec{\nabla} f \left[Q(t) - \frac{p_z^2}{E^2} \right]. \quad (17)$$

Assuming Bjorken's space-time picture of a central ultrarelativistic heavy-ion collision [34], we can use the relation

$$\frac{\vec{p}}{E} \cdot \vec{\nabla} f \approx \frac{p_z}{E} \frac{\partial f}{\partial z} = -\frac{p_z}{t} \frac{\partial f}{\partial p_z} \quad (18)$$

found in Ref. [9]. Inserting Eq. (18) into (17) and performing partial integrals we obtain

$$R_{\text{drift}}^{\text{tr}}(t) \approx \frac{-2}{[Q_{\text{eq}} - Q(t)] t} \left[Q(t) - \left\langle \frac{p_z^4}{E^4} \right\rangle (t) \right]. \quad (19)$$

Equation (19) shows that $R_{\text{drift}}^{\text{tr}}$ is negative, which agrees with our conclusion in the previous section. Using the approximation $\langle p_z^4/E^4 \rangle \approx Q^2$, we see that the larger the Q , the larger the $-R_{\text{drift}}^{\text{tr}}$.

B. R_{22}^{tr}

Changing p to p_1 , W_{22} becomes

$$W_{22}(t) = \frac{1}{n} \int \frac{d^3 p_1}{(2\pi)^3} \frac{p_{1z}^2}{E_1^2} C_{22}, \quad (20)$$

where C_{22} does not contribute to the second integral in Eq. (12) due to particle number conservation in elastic collisions. The same holds for the sum of C_{23} and C_{32} in chemical equilibrium. Inserting the explicit expression of the collision term

$$\begin{aligned} C_{22} = & \frac{1}{2E_1} \int d\Gamma_2 \frac{1}{2!} \int d\Gamma'_1 d\Gamma'_2 f'_1 f'_2 |\mathcal{M}_{1'2' \rightarrow 12}|^2 (2\pi)^4 \delta^{(4)}(p'_1 + p'_2 - p_1 - p_2) \\ & - \frac{1}{2E_1} \int d\Gamma_2 f_1 f_2 \frac{1}{2!} \int d\Gamma'_1 d\Gamma'_2 |\mathcal{M}_{12 \rightarrow 1'2'}|^2 (2\pi)^4 \delta^{(4)}(p_1 + p_2 - p'_1 - p'_2) \end{aligned} \quad (21)$$

($d\Gamma_i = d^3 p_i / (2\pi)^3 2E_i$ for short) into Eq. (20) gives two terms, which indicate the “gain” and “loss” in momentum isotropization.

The loss term is

$$\frac{1}{n} \int d\Gamma_1 d\Gamma_2 f_1 f_2 \frac{p_{1z}^2}{E_1^2} 2s \sigma_{22} = n \left\langle v_{\text{rel}} \frac{p_{1z}^2}{E_1^2} \sigma_{22} \right\rangle_2, \quad (22)$$

where

$$\sigma_{22} := \frac{1}{2s} \frac{1}{2!} \int d\Gamma'_1 d\Gamma'_2 |\mathcal{M}_{12 \rightarrow 1'2'}|^2 (2\pi)^4 \delta^{(4)}(p_1 + p_2 - p'_1 - p'_2) \quad (23)$$

is the total cross section, s is the invariant mass of the colliding system, $v_{\text{rel}} = s/2E_1 E_2$ is the relative velocity, and $\langle \rangle_2$ symbolizes an ensemble average over incoming particle pairs. In BAMPS $f(x, p) = \sum_i \delta^{(3)}[\vec{x} - \vec{x}_i(t)] \delta^{(3)}(\vec{p} - \vec{p}_i)$ and we evaluate the averages $\langle \rangle_2$ in local cells by running over all particle pairs in the cells. Each cell has a small volume to ensure local collisions and has a sufficient number of (test) particles to achieve adequate statistics.

The W_{22} 's gain term is $n \langle v_{\text{rel}} \tilde{\sigma}_{22} \rangle_2$, where

$$\tilde{\sigma}_{22} := \frac{1}{2s} \frac{1}{2!} \int d\Gamma'_1 d\Gamma'_2 \frac{p_{1z}^{\prime 2}}{E_1^{\prime 2}} |\mathcal{M}_{12 \rightarrow 1'2'}|^2 (2\pi)^4 \delta^{(4)}(p_1 + p_2 - p'_1 - p'_2), \quad (24)$$

which, like Eq. (23), is an integral over all possible states of outgoing particles. Equation (24) was obtained by exchanging the primed and unprimed variables in Eq. (21). Except for $p_{1z}^{\prime 2}/E_1^{\prime 2}$ all variables and functions in Eq. (24) are Lorentz invariant. Particularly we find $d\Gamma'_1 = d\Gamma_1^* = d^3 p_1^* / (2\pi)^3 2E_1^* = d\Omega^* dE_1^* E_1^* / 2(2\pi)^3$, where p_1^* is the four-momentum of an outgoing particle in the center-of-mass frame manifested by p_1 and p_2 of the incoming

particles, and Ω^* denotes the solid angle relative to the collision axis in the center-of-mass frame. Integrating over $d\Gamma'_2 = d\Gamma'^*_2$ using the four-dimensional δ function gives

$$\tilde{\sigma}_{22} = \int d\Omega^* \frac{d\sigma_{22}}{d\Omega^*} \frac{p'^2_{1z}}{E'^2_1}, \quad (25)$$

where p'_{1z} and E'_1 are the Lorentz transformed quantities from p^*_{1z} and, thus, functions of Ω^* , s , and $\vec{\beta}$. The $\vec{\beta} = (\vec{p}_1 + \vec{p}_2)/(E_1 + E_2)$ denotes the relative velocity of the center-of-mass frame of colliding particles to the laboratory frame where Q is defined.

We finally obtain

$$R^{\text{tr}}_{22} = \frac{W_{22}}{Q_{\text{eq}} - Q(t)} = \frac{1}{Q_{\text{eq}} - Q(t)} \left(n \left\langle v_{\text{rel}} \int d\Omega^* \frac{d\sigma_{22}}{d\Omega^*} \frac{p'^2_{1z}}{E'^2_1} \right\rangle_2 - n \left\langle v_{\text{rel}} \frac{p^2_{1z}}{E^2_1} \sigma_{22} \right\rangle_2 \right), \quad (26)$$

where the momentum isotropization gain and loss terms are clearly seen. The relationship to the collision-angle distribution is implicitly contained in R^{tr}_{22} . When the collision rate is defined as

$$R_{22} = n \langle v_{\text{rel}} \sigma_{22} \rangle_2, \quad (27)$$

then we call R^{tr}_{22} the *transport collision rate* of elastic scatterings.

The transport collision rate R^{tr}_{22} in Eq. (26), in general, differs from $n \langle v_{\text{rel}} \sigma^{\text{tr}}_{22} \rangle_2$, where σ^{tr}_{22} is defined in Eq. (1) or (2). They match only if the laboratory frame is identical to the center-of-mass frame of colliding particles. To demonstrate this we consider the special case in which half of the particles move along the positive z axis and the other half of the particles move along the negative z axis and all the particles have the same energy E such that

$$f(x, p) \propto \delta(p_x) \delta(p_y) \delta(p_z - E) + \delta(p_x) \delta(p_y) \delta(p_z + E). \quad (28)$$

In this case the laboratory frame is the same as the center-of-mass frame for every colliding pair. Thus $p'^2_{1z}/E'^2_1 = \cos^2 \theta^*$ and $p^2_{1z}/E^2_1 = 1$. We then have

$$R^{\text{tr}}_{22} = \frac{3}{2} n \langle v_{\text{rel}} \sigma^{\text{tr}}_{22} \rangle_2 \quad (29)$$

where σ^{tr}_{22} is given in Eq. (1). It is easy to verify that Eq. (29) does not depend on the direction of the initial momentum. The only necessary conditions are that all the particles move along the same (regardless of \pm sign) direction and have the same energy. Also, if $Q = \langle |p_z|/E \rangle$, R^{tr}_{22} will be changed to

$$R^{\text{tr}}_{22} = 2n \langle v_{\text{rel}} \sigma^{\text{tr}}_{22} \rangle_2, \quad (30)$$

where σ_{22}^{tr} is given in Eq. (2).

The reason R_{22}^{tr} is called as the transport collision rate now becomes obvious because Eq. (26) is the generalization of the simplified formula $n\sigma^{\text{tr}}$, which is referred to in the literature as the *transport collision rate* [7, 8].

To understand the physical meaning of the transport collision rate it is reasonable to interpret R_{22}^{tr} as the rate per particle at which particles experience elastic collisions to become isotropically distributed in momentum space, because R_{22}^{tr} contributes to momentum isotropization according to Eq. (15). For ultrarelativistic particles the inverse of R_{22}^{tr} is the mean path (or time) that particles should travel to become isotropic, and $R_{22}/R_{22}^{\text{tr}}$ is the average number of collisions, which each particle needs to drive the particle system into isotropy in momentum space.

To confirm this interpretation we calculate R_{22}^{tr} assuming that the collision angle is isotropically distributed. We then obtain $R_{22}^{\text{tr}} = R_{22}$ via Eq. (29) or (30) for the special case (28). This indicates that each particle needs only one collision to drive the particle system into isotropy in momentum space if the distribution of the collision angle is isotropic. A more general case occurs during equilibration. The energy spectrum of particles tends to be a Boltzmann distribution. Rarely found high-energy particles need on the average more than one collision to become isotropic, even if the distribution of the collision angle is isotropic. The reason is that a particle with high energy always collides with low-energy particles. The relative velocity of the center-of-mass frame to the laboratory frame is large and, thus, the Lorentz boost has a strong effect. In the laboratory frame deflection in the momentum of high-energy particles is narrower in the forward direction. However, low-energy particles move perpendicularly to their initial direction and, thus, their momentum deflection is large. The averaged effect of the Lorentz boost on the momentum isotropization is, however, nontrivial and must be calculated numerically.

The above hinges on the assumption that the system is static. Expanding systems are more complicated because particles flow. Collisions not only deflect the particle momenta but also force particles to flow. When we include the flow, which is the particle drift contribution to momentum isotropization [see Eq. (15)], the momentum degradation of flowing particles toward isotropy is slower ($\sim \theta_{\text{rel}}$) than the inverse of the transport collision rate, because the transport rate of particle drift is negative in an expanding system.

C. R_{23}^{tr} and R_{32}^{tr}

Compared with W_{22} in Eq. (20), W_{23} has an additional term due to particle production

$$W_{23}(t) = \frac{1}{n} \int \frac{d^3 p_1}{(2\pi)^3} \frac{p_{1z}^2}{E_1^2} C_{23} - Q(t) \frac{1}{n} \int \frac{d^3 p_1}{(2\pi)^3} C_{23}. \quad (31)$$

Inserting the explicit formula

$$C_{23} = \frac{1}{2E_1} \frac{1}{2!} \int d\Gamma_2 d\Gamma_3 \frac{1}{2!} \int d\Gamma'_1 d\Gamma'_2 f'_1 f'_2 |\mathcal{M}_{1'2' \rightarrow 123}|^2 (2\pi)^4 \delta^{(4)}(p'_1 + p'_2 - p_1 - p_2 - p_3) \\ - \frac{1}{2E_1} \int d\Gamma_2 f_1 f_2 \frac{1}{3!} \int d\Gamma'_1 d\Gamma'_2 d\Gamma'_3 |\mathcal{M}_{12 \rightarrow 1'2'3'}|^2 (2\pi)^4 \delta^{(4)}(p_1 + p_2 - p'_1 - p'_2 - p'_3) \quad (32)$$

into Eq. (31), we obtain

$$W_{23}(t) = \frac{3}{2} n \langle v_{\text{rel}} \tilde{\sigma}_{23} \rangle_2 - n \left\langle v_{\text{rel}} \frac{p_{1z}^2}{E_1^2} \sigma_{23} \right\rangle_2 - \frac{1}{2} Q(t) n \langle v_{\text{rel}} \sigma_{23} \rangle_2, \quad (33)$$

where

$$\tilde{\sigma}_{23} := \frac{1}{2s} \frac{1}{3!} \int d\Gamma'_1 d\Gamma'_2 d\Gamma'_3 \frac{p_{1z}^2}{E_1^2} |\mathcal{M}_{12 \rightarrow 1'2'3'}|^2 (2\pi)^4 \delta^{(4)}(p_1 + p_2 - p'_1 - p'_2 - p'_3). \quad (34)$$

The formula for σ_{23} is just Eq. (34), excluding p_{1z}^2/E_1^2 . The first two terms on the right-hand side of Eq. (33), the sum of which is equal to the first term on the right-hand side of Eq. (31), have similar forms as those in Eq. (26) [multiplying $Q_{\text{eq}} - Q(t)$] for W_{22} . The coefficients for the momentum isotropization gain and loss terms, 3/2 and 1, indicate that in a $2 \rightarrow 3$ collision the ratio of the gained to the lost particle number is 3/2. The last term in Eq. (33) stems from pure particle production. The coefficient for this term, 1/2, comes from the sum of the gain and loss terms in the particle production process. For a general $M \rightarrow N$ collision the coefficients will be N/M , 1, and $(N - M)/M$, respectively. Assuming that

$$\left\langle v_{\text{rel}} \frac{p_{1z}^2}{E_1^2} \sigma_{23} \right\rangle_2 \approx \left\langle \frac{p_{1z}^2}{E_1^2} \right\rangle \langle v_{\text{rel}} \sigma_{23} \rangle_2 = Q(t) \langle v_{\text{rel}} \sigma_{23} \rangle_2 \quad (35)$$

and then comparing W_{23} in Eq. (33) to W_{22} in Eq. (26) [multiplying $Q_{\text{eq}} - Q(t)$] we realize that a $gg \rightarrow ggg$ collision is a factor of 3/2 more efficient for momentum isotropization than a $gg \rightarrow gg$ collision, when $\sigma_{22} = \sigma_{23}$ and $\tilde{\sigma}_{22} = \tilde{\sigma}_{23}$. The physical reason is obvious: a $2 \rightarrow 3$ collision brings one more particle toward isotropy than a $2 \rightarrow 2$ collision.

For the special distribution function (28) we find a relation between the transport collision rate and the transport cross section (1)

$$R_{23}^{\text{tr}} = \frac{3}{2} \frac{3}{2} n \langle v_{\text{rel}} \sigma_{23}^{\text{tr}} \rangle_2. \quad (36)$$

For scattering processes with isotropically distributed collision angles one obtains $R_{23}^{\text{tr}} = \frac{3}{2} R_{23}$ where

$$R_{23} = n \langle v_{\text{rel}} \sigma_{23} \rangle_2 \quad (37)$$

denotes the collision rate for a gluon undergoing $gg \rightarrow ggg$ collisions. Bremsstrahlung effectively shortens the *mean transport path* of particles that are becoming isotropic in momentum space. Generally, in a $2 \rightarrow N$ process

$$R_{2N}^{\text{tr}} = \frac{N}{2} \frac{3}{2} n \langle v_{\text{rel}} \sigma_{2N}^{\text{tr}} \rangle_2 \quad (38)$$

and the larger the number N , the stronger the effect.

The final expression for W_{32} (intermediate steps are analogous to those for W_{23} , and C_{32} is found in Ref. [5]) is given by

$$W_{32}(t) = \frac{1}{3} n^2 \left\langle \frac{\tilde{I}_{32}}{8E_1 E_2 E_3} \right\rangle_3 - \frac{1}{2} n^2 \left\langle \frac{p_{1z}^2}{E_1^2} \frac{I_{32}}{8E_1 E_2 E_3} \right\rangle_3 + \frac{1}{6} Q(t) n^2 \left\langle \frac{I_{32}}{8E_1 E_2 E_3} \right\rangle_3, \quad (39)$$

where

$$\tilde{I}_{32} := \frac{1}{2!} \int d\Gamma'_1 d\Gamma'_2 \frac{p_{1z}'^2}{E_1'^2} |\mathcal{M}_{123 \rightarrow 1'2'}|^2 (2\pi)^4 \delta^{(4)}(p_1 + p_2 + p_3 - p'_1 - p'_2). \quad (40)$$

I_{32} is just Eq. (40), excluding $p_{1z}'^2/E_1'^2$. $\langle \rangle_3$ denotes an ensemble average over triplets of incoming particles.

Comparing W_{23} to W_{32} , we see that the sum of the last terms in Eqs. (33) and (39) originates from the second term in Eq. (12) but substituting $C_{23} + C_{32}$ in for $\partial f / \partial t$ and it should be zero at chemical equilibrium. We obtain

$$n \langle v_{\text{rel}} \sigma_{23} \rangle_2 = \frac{1}{3} n^2 \left\langle \frac{I_{32}}{8E_1 E_2 E_3} \right\rangle_3 \quad (41)$$

or, equivalently, $R_{23} = \frac{2}{3} R_{32}$, where

$$R_{32} = \frac{1}{2} n^2 \left\langle \frac{I_{32}}{8E_1 E_2 E_3} \right\rangle_3. \quad (42)$$

From Eq. (41) we derived the collision rate of a gluon experiencing $ggg \rightarrow gg$ collisions.

Assuming that

$$\left\langle \frac{p_{1z}^2}{E_1^2} \frac{I_{32}}{8E_1 E_2 E_3} \right\rangle_3 \approx Q(t) \left\langle \frac{I_{32}}{8E_1 E_2 E_3} \right\rangle_3 \quad (43)$$

we finally have

$$\begin{aligned} W_{23}(t) &\approx \frac{3}{2} (n \langle v_{\text{rel}} \tilde{\sigma}_{23} \rangle_2 - Q(t) n \langle v_{\text{rel}} \sigma_{23} \rangle_2) \\ W_{32}(t) &\approx \frac{1}{3} n^2 \left\langle \frac{\tilde{I}_{32}}{8E_1 E_2 E_3} \right\rangle_3 - Q(t) \frac{1}{3} n^2 \left\langle \frac{I_{32}}{8E_1 E_2 E_3} \right\rangle_3. \end{aligned}$$

The expansion together with Eq. (41) leads to $W_{23} \approx \frac{3}{2}W_{32}$ and $R_{23}^{\text{tr}} \approx \frac{3}{2}R_{32}^{\text{tr}}$ for chemical equilibrium. Thus, a $2 \rightarrow 3$ process should contribute more to kinetic equilibration than a $3 \rightarrow 2$ process because it brings one more particle toward isotropy. If the system is out of chemical equilibrium, one expects $R_{23}^{\text{tr}} \approx \frac{3}{2} \frac{1}{\lambda_g} R_{32}^{\text{tr}}$, where the gluon fugacity $\lambda_g = 1$ at chemical equilibrium. In an undersaturated system ($\lambda_g < 1$), for instance, particle production dominates and, therefore, R_{23}^{tr} is much larger than R_{32}^{tr} .

For the special case (28) there is a direct relation between the transport collision rate and transport cross section [see Eqs. (29) and (36)]. The same should be self-evident for R_{32}^{tr} when detailed balance is considered

$$R_{32}^{\text{tr}} \approx \frac{2}{3} \lambda_g R_{23}^{\text{tr}} = \frac{3}{2} \lambda_g n \langle v_{\text{rel}} \sigma_{23}^{\text{tr}} \rangle_2. \quad (44)$$

If the distribution of the collision angle is isotropic, $R_{32}^{\text{tr}} \approx \lambda_g R_{23} = \frac{2}{3} R_{32}$, where $\lambda_g = 2R_{32}/3R_{23}$ is used. For a $N \rightarrow 2$ collision ($N > 2$)

$$R_{N2}^{\text{tr}} \approx \frac{2}{N} \lambda_g R_{2N}^{\text{tr}} = \frac{3}{2} \lambda_g n \langle v_{\text{rel}} \sigma_{2N}^{\text{tr}} \rangle_2, \quad (45)$$

which is not proportional to N in contrast to R_{2N}^{tr} in Eq. (38). For large N a $2 \rightarrow N$ process kinetically equilibrates significantly more efficiently.

We summarize the main findings derived in this section:

- (i) In Eq. (15) we showed that the relaxation rate of momentum isotropization is a sum of the *transport rate* of particle drift and the *transport collision rates* of the various scattering processes.
- (ii) The transport rate of particle drift is negative for an expanding medium, which means that the particle drift counteracts the momentum isotropization.
- (iii) The transport collision rates of the various interactions found in Eqs. (26), (33), and (39) [over $Q_{\text{eq}} - Q(t)$] have indirect but correctly implemented relationships with the collision-angle distributions.
- (iv) $2 \rightarrow N$ ($N > 2$) processes isotropize the momentum more efficiently than elastic collisions or annihilation processes because the production process brings more than two particles toward isotropy in momentum space.

(v) The relations between the transport collision rates and the transport cross sections for the special case in (28)

$$R_{22}^{\text{tr}} = \frac{3}{2} n \langle v_{\text{rel}} \sigma_{22}^{\text{tr}} \rangle_2, \quad R_{23}^{\text{tr}} = \frac{3}{2} \frac{3}{2} n \langle v_{\text{rel}} \sigma_{23}^{\text{tr}} \rangle_2, \quad R_{32}^{\text{tr}} \approx \frac{3}{2} \lambda_g n \langle v_{\text{rel}} \sigma_{23}^{\text{tr}} \rangle_2 \quad (46)$$

are found as long as $Q = \langle p_z^2/E^2 \rangle$ and the transport cross section is defined by Eq. (1). However, if $Q = \langle |p_z|/E \rangle$ and the transport cross section is defined by Eq. (2),

$$R_{22}^{\text{tr}} = 2 n \langle v_{\text{rel}} \sigma_{22}^{\text{tr}} \rangle_2, \quad R_{23}^{\text{tr}} = \frac{3}{2} 2 n \langle v_{\text{rel}} \sigma_{23}^{\text{tr}} \rangle_2, \quad R_{32}^{\text{tr}} \approx 2 \lambda_g n \langle v_{\text{rel}} \sigma_{23}^{\text{tr}} \rangle_2. \quad (47)$$

For the isotropic distribution of the collision angle we find

$$R_{22}^{\text{tr}} = R_{22}, \quad R_{23}^{\text{tr}} = \frac{3}{2} R_{23}, \quad R_{32}^{\text{tr}} \approx \frac{2}{3} R_{32}. \quad (48)$$

VI. RESULTS FROM THE PARTON CASCADE CALCULATIONS

In this section we present results on the gluon transport rates in the central region of the expansion simulated by BAMPS. We then compare the transport rates with those obtained from the standard concept of the transport cross sections. The potential dependence of the relaxation time on momentum is determined.

A. Transport rate

In Fig. 7 $-R_{\text{drift}}^{\text{tr}}$ is shown. It cannot be computed by Eq. (17) because of strong numerical uncertainties in calculating $\vec{\nabla} f$. Instead, it is obtained by summing $\pm[Q(t) - p_z^2/E^2]$ over the particles, which come into (+ sign) as well as leave (- sign) the central region within a time interval of 0.1 fm/c. This causes a large statistical fluctuation. Comparing Fig. 6 to Fig. 7 we realize that the larger the $Q = \langle p_z^2/E^2 \rangle$, the larger is the (negative) effect of the particle drift on momentum isotropization. This confirms our qualitative understanding outlined in Sec. IV. The dotted curves estimate the transport rate according to Eq. (19) assuming a one-dimensional Bjorken boost-invariance expansion. $Q(t)$ and $\langle p_z^4/E^4 \rangle(t)$ come from the parton cascade. At intermediate times our estimates nicely match the numerical results, which indicates that the expansion follows a Bjorken expansion. Early in the expansion the particle drift is stronger due to free streaming caused by the initial conditions. Later on the expansion becomes three-dimensional and particles begin to flow outward in the

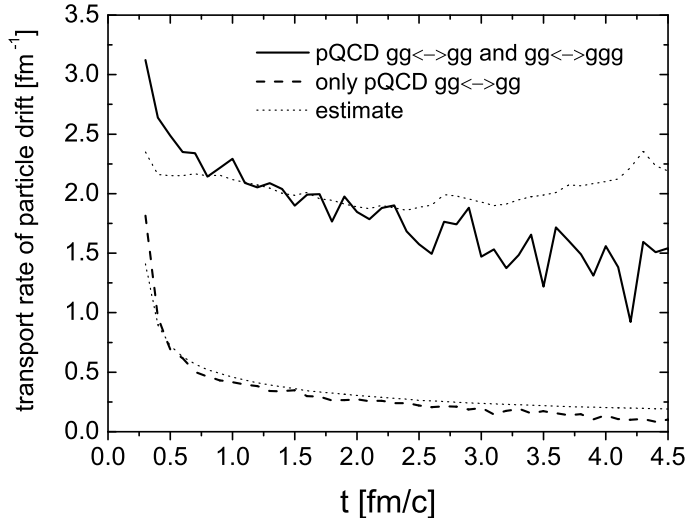


FIG. 7: Particle drift transport rate (multiplied by -1) from both elastic and inelastic pQCD-scattering processes (solid curve), from elastic-only pQCD-scattering processes (dashed curve), and from estimates in Eq. (19) (dotted curves).

transverse direction. The transverse drift of particles with large p_T is then similar to the longitudinal drift of particles with large $p_z \sim p_T$. The net effect of the particle drift on momentum isotropization in a three-dimensional expansion diminishes in comparison to a purely longitudinal expansion, as demonstrated in Fig. 7 with the comparison of the numerical results to the estimations.

The numerical results for the transport collision rates are calculated using the expressions (26), (33), and (39) {the last two are divided by $[Q_{\text{eq}} - Q(t)]$ }, and are shown in Fig. 8. One realizes the dominance of the inelastic collisions in momentum isotropization by computing the ratio $(R_{23}^{\text{tr}} + R_{32}^{\text{tr}})/R_{22}^{\text{tr}}$, which is about 5 throughout the entire evolution of the system. The ratio of R_{23}^{tr} to R_{32}^{tr} is always larger than $3/2$ but nears $3/2$ late in the expansion. According to Eq. (44) the system is undersaturated early on and eventually reaches chemical equilibrium. When we compare R_{22}^{tr} s obtained from the various simulations, the difference is small, unlike for the cross sections shown in Fig. 4. The reason lies in the difference in the evolution of the Debye screening mass for the various simulations as shown in Fig. 5. A smaller Debye screening mass leads to a larger cross section but also a smaller collision angle. The former causes more frequent collisions and, thus, speeds up equilibration, whereas the latter causes inefficient momentum deflection and, thus, slows equilibration. Both contribute

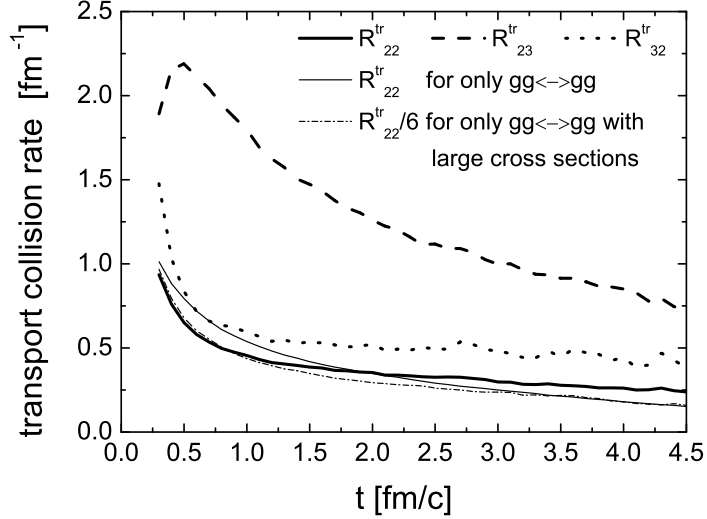


FIG. 8: Transport collision rates (R_{22}^{tr} , R_{23}^{tr} and R_{32}^{tr}) from both elastic and inelastic pQCD-scattering processes (thick solid, thick dashed, and thick dotted curve, respectively), R_{22}^{tr} from elastic-only pQCD scatterings (thin solid curve) and $R_{22}^{\text{tr}}/6$ from elastic-only processes using artificially large cross sections (thin dash-dotted curve).

to the transport collision rate so that it is not particularly sensitive to the Debye screening mass unlike the total cross section. In Fig. 4 the total cross sections for elastic collisions differ by a factor of 4 – 6 between elastic-only scatterings and those that include bremsstrahlung processes, whereas the corresponding transport collision rates in Fig. 8 are nearly identical.

The ratios of elastic+inelastic scatterings to elastic-only collisions for the total transport collision rate and the transport rate of particle drift are almost identical: the ratio increases from 4 at 0.3 fm/c to 9 at 4.5 fm/c. The inverse of the ratio of the momentum isotropization time scales in the two simulations is also the same (see Fig. 11).

Because the change in particle drift is a consequence of particle collisions, one may expect that the momentum isotropization is dependent only on the total transport collision rate. Gluon kinetic equilibration would always look the same, if the total transport collision rate in every evolution was the same at every space-time point. The types of collision processes are not relevant, although they are interesting in their own right. We have already shown two examples of evolution of gluons in a central Au+Au collision at RHIC energy. The total transport collision rate becomes on average a factor of 6 larger if pQCD bremsstrahlung processes are included. For another evolution to have the same total transport collision rate

as that obtained when pQCD bremsstrahlung processes are included, elastic-only scattering processes with larger cross sections, namely $d\sigma_{22}/d\hat{t} = 6 d\sigma_{22}^{\text{pQCD}}/d\hat{t}$, were used. If the elastic pQCD cross sections obtained from the new simulation were the same as those from elastic-only scatterings with pQCD cross sections (see the dotted curve in Fig 4), 6 would be an appropriate prefactor. The dash-dotted curve in Fig. 4 shows the elastic pQCD cross section calculated from the new simulation, which is a factor of 2 smaller than the dotted curve. Recalling that the cross sections are dependent on the development of the Debye screening mass and that the gluon evolution resembles free streaming for elastic-only pQCD scatterings when the Debye screening mass decreases as $\sim t^{-1/2}$, artificially large cross sections decrease the Debye screening mass from $t^{-1/2}$ to $t^{-1/3}$ (see the dash-dotted curve in Fig. 5), which implies that the evolution of gluons for large cross sections is a hydrodynamical expansion with a finite viscosity.

$R_{22}^{\text{tr}}/6$ for large cross sections is depicted in Fig. 8 and is nearly the same as the transport collision rate for standard pQCD cross sections, which proves that the transport collision rate for elastic pQCD scatterings is not sensitive to the Debye screening mass. Therefore, the total transport collision rates for elastic-only collisions with large cross sections and for both elastic and inelastic pQCD scatterings are nearly the same, which implies the same momentum isotropization in both simulations. Comparing the time evolution of the momentum isotropization (the solid versus the dash-dotted curve in Fig. 6), we realize that momentum isotropization is indeed nearly the same. However, the total cross sections are very different (see Fig. 4). At 4.5 fm/c, for instance, $\langle\sigma_{22}\rangle_2 + \langle\sigma_{23}\rangle_2 \approx 4$ mb for elastic and inelastic scatterings, whereas $\langle\sigma_{22}\rangle_2 \approx 45$ mb for elastic-only collisions, which is a factor of 12 larger!

Because kinetic equilibration and pressure buildup are related we also expect that pressure buildup does not depend on the type of interactions. Figure 9 shows the time evolution of the transverse energy per unit momentum rapidity at midrapidity. The decrease in the transverse energy indicates that mechanical work has been done by pressure gradients, which are built up during kinetic equilibration. From Fig. 9 one realizes that the time evolution of $dE_T/dy|_{y=0}$ obtained from elastic and inelastic scatterings and from elastic-only scatterings with large cross sections are almost identical. This indicates that the ongoing kinetic equilibration and the pressure gradients buildup are the same not only at the collision center as already shown in Fig. 6 but also at the central slice of the expansion. There only the total

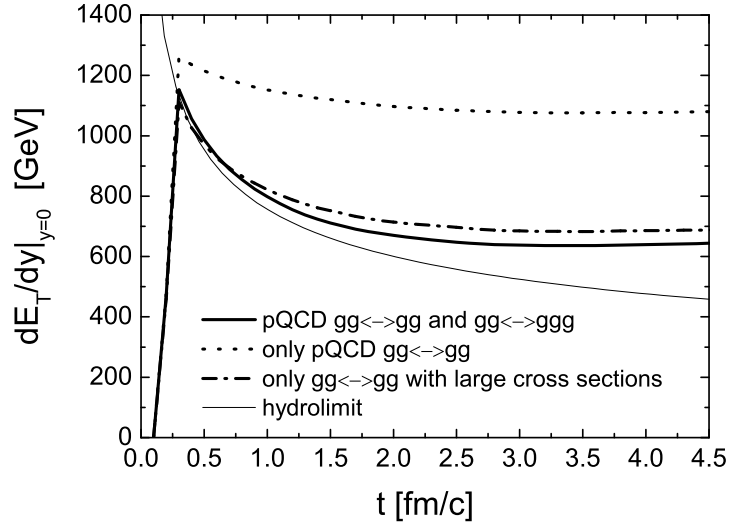


FIG. 9: Time evolution of the transverse energy per unit momentum rapidity at midrapidity for both elastic and inelastic pQCD scatterings (solid curve), for elastic-only pQCD scatterings (dotted curve), for elastic-only scatterings with large cross sections (dash-dotted curve), and the ideal hydrolimit, $dE_T/dy|_{y=0} \sim t^{-1/3}$ (thin solid curve).

transport collision rate matters, not the detail of the interactions.

Whereas the decrease in $dE_T/dy|_{y=0}$ for elastic-only pQCD collisions is very weak, which implies slow momentum isotropization, the decrease in $dE_T/dy|_{y=0}$ in the other two is close to the ideal hydrodynamic limit at least until 1.5 fm/c. Later the expansion becomes three-dimensional and gluons in the outer regions cease to interact when the energy density decreases under the critical value of $1 \text{ GeV}/\text{fm}^3$. Therefore, the decrease in the transverse energy slows so that the final value of $dE_T/dy|_{y=0}$ is about 650 GeV, which is comparable with RHIC data [33].

Although the interaction details do not matter for kinetic equilibration and pressure buildup, they do for chemical equilibration. Elastic collisions conserve the absolute particle number and do not contribute to chemical equilibration, whereas multiplication and annihilation processes can drive systems toward chemical equilibrium. For the gluon evolution in central Au+Au collisions the initial free streaming (or the off-shell propagation) undersaturates the gluons (see Fig. 15). For the pQCD bremsstrahlung processes chemical equilibrium is achieved by producing gluons. This leads to a larger Debye screening mass than that for elastic-only collisions (see Fig. 5). Therefore, the elastic pQCD cross section

obtained from the simulation including the pQCD bremsstrahlung processes is the smallest (see Fig. 4).

B. Mean free path, mean transport path, and relaxation time

Figure 10 shows the mean free path and the *mean transport path* of gluons. The *mean*

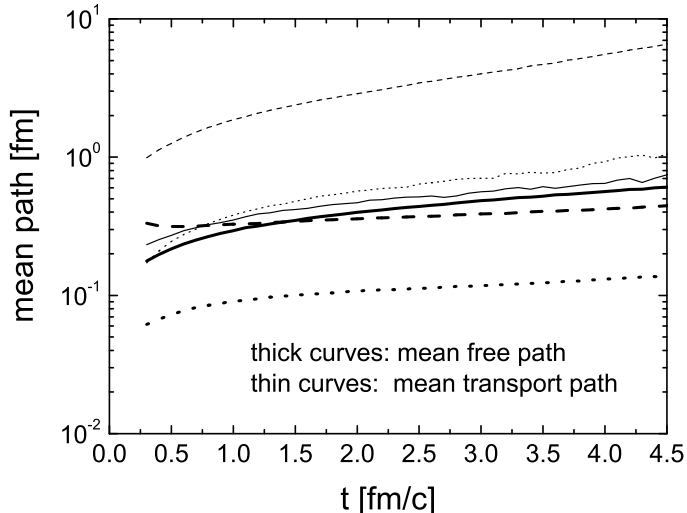


FIG. 10: Mean free path and mean transport path of gluons for both elastic and inelastic pQCD scatterings (solid curves), for elastic-only pQCD scatterings (dashed curves) and for elastic-only collisions with artificially large cross sections (dotted curves).

transport path is defined as the inverse of the total transport collision rate and it is the path needed for gluons to reach isotropy in momentum space in a static medium. From Fig. 10 we see that the mean paths are all small early on and increase throughout the course of the expansion when the system becomes dilute. Comparing the mean free paths there is little difference for the processes with and without pQCD bremsstrahlung; however, the mean free path is much smaller when artificially large cross sections are considered. We also see that the mean transport path is larger than the mean free path for elastic-only collisions, because elastic pQCD collisions have small-angle scatterings and, therefore, do not isotropize the momentum efficiently. However, when pQCD bremsstrahlung processes are included the mean transport path and the mean free path are quite similar, so their kinetic equilibration is efficient.

The relaxation rate of momentum isotropization $1/\theta_{\text{rel}}(t)$ is calculated directly from Fig.

6 using Eq. (9) and is shown in Fig. 11 in comparison with the total transport rate $R_{\text{drift}}^{\text{tr}} + R_{22}^{\text{tr}} + R_{23}^{\text{tr}} + R_{32}^{\text{tr}}$. According to Eq. (15) they should be identical, which is indeed

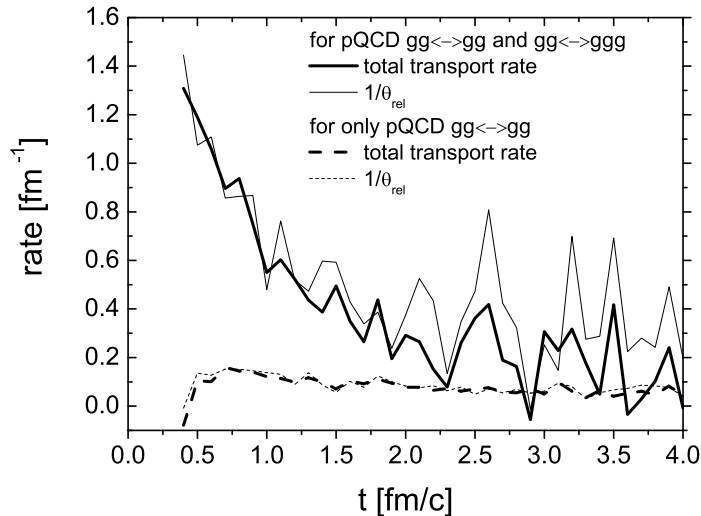


FIG. 11: Relaxation rate of momentum isotropization compared with the total transport rate for both elastic and inelastic pQCD scatterings (thin and thick solid curves) and for elastic-only pQCD scatterings (thin and thick dashed curves).

seen within the numerical uncertainty. This indicates that the transport rates were correctly extracted. For the first 2 fm/c of the gluon evolution for pQCD bremsstrahlung processes the time scale of momentum isotropization is 1 – 2 fm/c, which is about a factor of 5 times larger than the mean free path (see Fig. 10).

C. Collision rate, transport collision rate, and transport cross section

Here we compare the collision rates, the transport collision rates and the estimates using the transport cross sections with each other concentrating on the results from the simulation with both elastic and inelastic collisions.

Assuming Eq. (28), the transport collision rates are directly proportional to the transport cross sections [see Eqs. (46), (47), and (48)], which can be directly linked to the collision angle distribution. To see how they differ from the true transport collision rates we compare the transport collision rates, $n\langle v_{\text{rel}} \sigma^{\text{tr}} \rangle$ and the collision rates in Fig. 12. Multiplication factors according to Eqs. (46) and (48) allow for more convenient comparisons. If the assumption (28) is realistic, the curves according to the assumption and those for the true transport

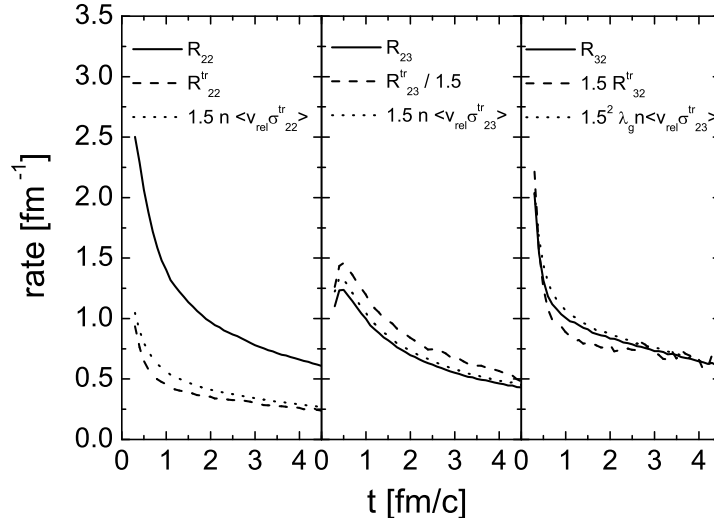


FIG. 12: Collision rate, transport collision rate, and $n\langle v_{\text{rel}}\sigma^{\text{tr}}\rangle$ of the various collision processes. The results are obtained from the simulation, including both elastic and inelastic pQCD-scattering processes, and are depicted by the solid, dashed, and dotted curves, respectively.

collision rate are identical. If additionally the collision-angle distribution is isotropic, all the curves in each case lie on top of each other. The fugacity λ_g in Eq. (46) is calculated by $\lambda_g = n/n_{\text{eq}}$, where $n_{\text{eq}} = 16T^3/\pi^2$ is the gluon density at thermal equilibrium at temperature $T \equiv \epsilon/3n$. The gluon density n and energy density ϵ are extracted from the parton cascade.

We first examine the rates for the elastic-scattering processes shown on the left in Fig. 12, where there is only a small difference between the true transport collision rate and the reduced rate related to the transport cross section. The difference comes from the Lorentz boost from the center-of-mass frame to the laboratory frame. Furthermore, we see that the transport collision rate is much smaller than the collision rate, which is again due to the fact that the pQCD $gg \rightarrow gg$ scatterings are small-angle scatterings and are not efficient for momentum isotropization.

In the middle the rates for the $gg \rightarrow ggg$ bremsstrahlung processes are shown where little difference is seen. The transport collision rate divided by the kinematic factor $3/2$ is the largest rate, especially over the collision rate. The kinematic factor for the assumption (28) is exactly $3/2$. However, in general it is only approximately equal to $3/2$, because the decomposition (35) for R_{23}^{tr} [see W_{23}^{tr} in Eq. (33)] is an approximation. The real kinematic

factor defined as A may be larger than $3/2$, which would lower R_{23}^{tr}/A below R_{23} . Even though the difference between $\frac{2}{3}R_{23}^{\text{tr}}$ and R_{23} is small, which indicates that the collision-angle distribution in $gg \rightarrow ggg$ collisions is nearly isotropic. The same is also seen on the right in Fig. 12, where the rates for $ggg \rightarrow gg$ are nearly identical.

Figure 12 shows that the reduced transport collision rates related to the transport cross sections do not differ very much from the derived transport collision rates. Generally, the Lorentz boost from the individual center-of-mass frame to the laboratory frame does not lead to a big effect on momentum isotropization. This is nontrivial. However, it provides a basis to understand thermalization within multiparticle reactions. Additionally, the transport collision rates derivation helps to obtain the *kinematic* factors in Eq. (46), which are essential in quantitative analyses but typically ignored in the literature [7, 8].

Bremsstrahlung processes $gg \leftrightarrow ggg$ are suppressed by the LPM effect, which occurs when a parton undergoes multiple scatters with radiated gluons through a QCD medium (originally photons in the QED medium). The interference of radiated gluons leads to suppression of radiation of gluons with modes (w, \vec{k}) , where w and \vec{k} denote the gluon's energy and momentum. Heuristically, there is no suppression for gluons with a *formation time* $\tau = w/k_T^2$ smaller than the mean free path. This is called the Bethe-Heitler limit, where the gluon radiation induced at different space-time points in the course of the propagation of a parton can be considered as independent events. Events within the Bethe-Heitler regime are included in BAMPS. Other gluon modes radiation with coherent suppression completely drops out, which is the reason for the Θ function in the matrix element in Eq. (4). Including these events speeds up thermalization; however, implementing the coherent effect into a transport model where the Boltzmann equation is solved remains a challenge.

Without implementing the LPM effect as a strict low momentum cutoff, the matrix element for $gg \leftrightarrow ggg$ in Eq. (4) is dominated by collinear bremsstrahlung, although it is suppressed by the Debye screening mass as an infrared cutoff. Therefore, the larger collision angle from $gg \leftrightarrow ggg$ processes in comparison to elastic scatterings originates from the present implementation of the LPM effect.

Because the angle of the radiated gluon relative to the collision axis θ is related to the momentum rapidity y by $\cos \theta = \tanh y$, which leads to $\cosh y = 1/\sin \theta$, the effect of the Θ function in the matrix element (4), $\Theta(k_{\perp}\Lambda_g - \cosh y)$, on the angular distribution of the radiated gluon can be understood. For small transverse momentum k_{\perp} , which the radiation

favours, the rapidity y is small due to the Θ function if the mean free path Λ_g is small. This leads to large-angle radiation. The larger Λ_g , the more small-angle bremsstrahlung (with large y) occurs.

The Θ function results in a cutoff in the radiated gluon phase space. The corresponding total cross section is found by integrating the matrix element

$$\sigma_{gg \rightarrow ggg} \sim \int_0^{1/4} d\bar{q}_\perp^2 \int_{1/\bar{\Lambda}_g^2}^{1/4} d\bar{k}_\perp^2 \int_{-y_m}^{y_m} dy \int_0^\pi d\phi \frac{1}{(\bar{q}_\perp^2 + \bar{m}_D^2)^2} \frac{\bar{q}_\perp^2}{\bar{k}_\perp^2 [(\bar{\mathbf{k}}_\perp - \bar{\mathbf{q}}_\perp)^2 + \bar{m}_D^2]} H(\bar{q}_\perp, \bar{k}_\perp, y, \phi), \quad (49)$$

where $\bar{q}_\perp^2 = q_\perp^2/s$, $\bar{k}_\perp^2 = k_\perp^2/s$, $\bar{\Lambda}_g = \Lambda_g \sqrt{s}$, $\bar{m}_D^2 = m_D^2/s$, ϕ is the angle between \mathbf{k}_\perp and \mathbf{q}_\perp , and H is a function of \bar{q}_\perp , \bar{k}_\perp , y , and ϕ . H (found in Appendix D of Ref. [5]) appears after the integral over the radiating gluon momentum. In Eq. (49) the lower cutoff for k_\perp and the upper (lower) cutoff $\pm y_m$ for y can be seen, where y_m is the minimum among $\text{arcosh}(\bar{k}_\perp \bar{\Lambda}_g)$ and $\text{arcosh}(1/2\bar{k}_\perp)$ (see Appendix D of Ref. [5]). To obtain the radiated gluon angular distribution, which depends on \bar{m}_D^2 and $\bar{\Lambda}_g$, one has to integrate over \bar{k}_\perp , ϕ and \bar{q}_\perp in Eq. (49). This is already done in Ref. [5]. The radiated gluon angular distribution and the distributions of the other two gluons were depicted in Fig. 49 in Ref. [5], where $\bar{m}_D^2 = 0.05$ and $\bar{\Lambda}_g = 4$. The distributions are nearly isotropic. From the present BAMPS calculation $\bar{m}_D^2 \approx 0.1$ and $\bar{\Lambda}_g \approx 3$ when pQCD bremsstrahlung is included. The value of \bar{m}_D^2 is almost identical with the equilibrium value $m_D^2/\langle s \rangle = 4\alpha_s/3\pi = 0.13$ for $\alpha_s = 0.3$. The smaller \bar{m}_D^2 found in Ref. [5] is due to the slower chemical equilibration, because the initial system (using $p_0 = 2$ GeV) is more dilute than that used in this article (using $p_0 = 1.4$ GeV). For larger \bar{m}_D^2 and smaller $\bar{\Lambda}_g$ large-angle scatterings for $gg \rightarrow ggg$ are favored.

Because the radiation is dominated by $1/\bar{k}_\perp^2$ we simplify the matrix element (4) by eliminating the collinear term $1/[(\bar{\mathbf{k}}_\perp - \bar{\mathbf{q}}_\perp)^2 + \bar{m}_D^2] \sim 1/\bar{m}_D^2$ to see the effect of the LPM suppression (Bethe-Heitler regime) on the radiated gluon angular distribution. Then the radiation can be factorized

$$\begin{aligned} \sigma_{gg \rightarrow ggg} &\sim \int_{1/\bar{\Lambda}_g}^{1/2} d\bar{k}_\perp \int_{-y_m}^{y_m} dy \frac{1}{\bar{k}_\perp} = \int_{-\text{arcosh}\sqrt{\bar{\Lambda}_g/2}}^{\text{arcosh}\sqrt{\bar{\Lambda}_g/2}} dy \int_{\cosh y/\bar{\Lambda}_g}^{1/2 \cosh y} d\bar{k}_\perp \frac{1}{\bar{k}_\perp} \\ &= \int_{-\text{arcosh}\sqrt{\bar{\Lambda}_g/2}}^{\text{arcosh}\sqrt{\bar{\Lambda}_g/2}} dy \ln \frac{\bar{\Lambda}_g}{2 \cosh^2 y} = \int_{-\sqrt{1-2/\bar{\Lambda}_g}}^{\sqrt{1-2/\bar{\Lambda}_g}} du \frac{\ln[\bar{\Lambda}_g(1-u^2)/2]}{1-u^2}, \end{aligned} \quad (50)$$

where $u = \cos \theta$. The integrand approximately represents the radiated gluon angular distribution, which is bounded by $\pm \sqrt{1-2/\bar{\Lambda}_g}$. Figure 13 shows the distribution for various $\bar{\Lambda}_g = \Lambda_g \sqrt{s} \sim \Lambda_g T$. The distributions are normalized and symmetric in $\cos \theta$. The angular

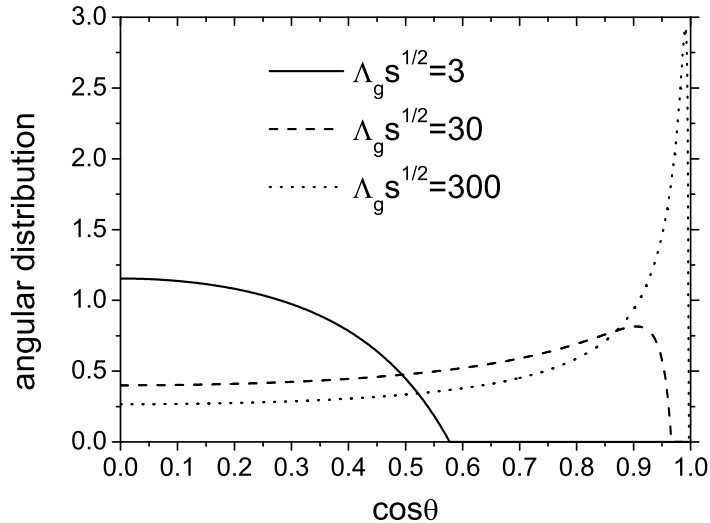


FIG. 13: Radiated gluon angular distribution in the center-of-mass frame.

distribution is peaked in the forward direction only for large $\bar{\Lambda}_g$ as in elastic scatterings. In BAMPS we find $\bar{\Lambda}_g \approx 3$. Therefore, the radiated gluon angular distribution according to Eq. (49) is similar to $\Lambda_g \sqrt{s} = 3$ in Fig. 13, which indicates that large-angle radiation is favored.

D. Dependence of the transport rate on the definition of Q

We have already mentioned that the transport rates depend on the definition of the degree of momentum isotropy Q . In the previous subsections the numerical results for the transport rates with $Q = \langle p_z^2/E^2 \rangle$ were shown. But the dependence of the numerical results of the transport rates on Q (specially when it is set to $Q = \langle |p_z|/E \rangle$) remains to be calculated.

Reasonable definitions of Q must consider some kind of average of the momentum spectra shown in Fig. 2; thus, momentum isotropization time scales obtained from different prescriptions cannot differ much from each other. Because the inverse of the total transport rate is the momentum isotropization time scale, we do not expect any significant dependence of the transport rate on the definition of Q .

Here we first compare the transport collision rates in the reduced formulas (46) for $Q = \langle p_z^2/E^2 \rangle$ with those in Eq. (47) for $Q = \langle |p_z|/E \rangle$, where transport cross sections are defined by (1) and (2), respectively. We have already shown that if the collision angle is isotropically distributed, the transport collision rates of a certain type of scattering processes are the

same, regardless of the definition of Q . For small-angle scatterings one has $\sin^2 \theta \approx \theta^2$ and $1 - \cos \theta \approx \theta^2/2$, and the transport collision rates for $Q = \langle p_z^2/E^2 \rangle$ are a factor of 1.5 larger than those when $Q = \langle |p_z|/E \rangle$. For large-angle scatterings $\sin^2 \theta \approx 1 - \cos \theta$ and then the transport collision rates for $Q = \langle p_z^2/E^2 \rangle$ are in turn a factor of 3/4 smaller than those when $Q = \langle |p_z|/E \rangle$. The maximal relative difference amounts to 50%. Because pQCD bremsstrahlung is the dominant process in kinetic equilibration and the collision angle for that process is roughly isotropic due to the LPM cutoff, the difference in the transport collision rates due to different Q s should be minimal.

Figure 14 shows the numerical results for the transport rates with the Q s defined above. The differences are only small, which means that the transport rates are not dependent on

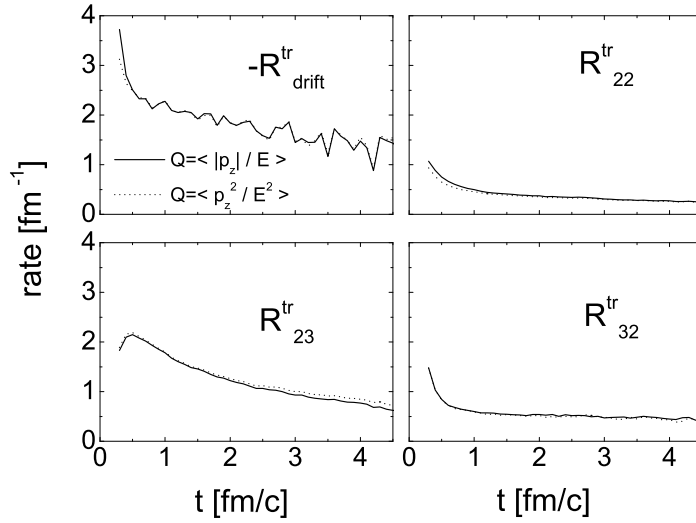


FIG. 14: Transport rates calculated with $Q = \langle |p_z|/E \rangle$ (solid curves) and $Q = \langle p_z^2/E^2 \rangle$ (dotted curves).

our choice in Q .

E. Relaxation time τ_{rel} in the relaxation time approximation

The collision term of the Boltzmann equation (13) can be written as

$$C(x, p) = \frac{f_{\text{eq}}(x, p) - f(x, p)}{\tau_{\text{rel}}(x, p)}, \quad (51)$$

which describes the relaxation of the particle-density function $f(x, p)$ by using a space-time and momentum-dependent *relaxation time* $\tau_{\text{rel}}(x, p)$, where $\tau_{\text{rel}}(x, p)$ is a functional of $f(x, p)$.

The underlying approximation in the so-called *relaxation time ansatz* is the *ignorance* of the momentum dependence of the relaxation time, i.e., $\tau_{\text{rel}}(x, p) \approx \tau_{\text{rel}}(x)$. Thus, $\tau_{\text{rel}}(x)$ gives the time scale of the overall equilibration in absence of particle drift, which was used in [9, 10, 11, 12, 13, 14, 15] to calculate the time scale of thermalization within various dynamical scenarios of the expansion. It is crucial to see whether τ_{rel} in the relaxation time approximation is equivalent to the mean transport path, because the latter determines the momentum isotropization time scale in a static system.

For kinetic equilibration we insert (51) into the time derivative of the momentum isotropization (12) and obtain [by dividing $(Q_{\text{eq}} - Q)$]

$$\begin{aligned} R_{22}^{\text{tr}} + R_{23}^{\text{tr}} + R_{32}^{\text{tr}} &= \frac{1}{Q_{\text{eq}} - Q} \left(\frac{1}{n} \int \frac{d^3p}{(2\pi)^3} \frac{p_z^2}{E^2} \frac{f_{\text{eq}} - f}{\tau_{\text{rel}}} - Q(t) \frac{1}{n} \int \frac{d^3p}{(2\pi)^3} \frac{f_{\text{eq}} - f}{\tau_{\text{rel}}} \right) \\ &= \frac{1}{Q_{\text{eq}} - Q} \left(\frac{n_{\text{eq}} Q_{\text{eq}} - n Q}{n \langle \tau_{\text{rel}} \rangle_k} - Q \frac{n_{\text{eq}} - n}{n \langle \tau_{\text{rel}} \rangle_c} \right), \end{aligned} \quad (52)$$

where $\langle \tau_{\text{rel}} \rangle_k$ and $\langle \tau_{\text{rel}} \rangle_c$ are defined as averaged quantities over the momentum, and the index k denotes kinetic equilibration due to the convolution of angles (p_z^2/E^2) in the first integration, whereas c denotes chemical equilibration.

$\langle \tau_{\text{rel}} \rangle_c$ can also be calculated by integrating the collision term of the Boltzmann equation over the momentum

$$\int \frac{d^3p}{(2\pi)^3} (C_{22} + C_{23} + C_{32}) = \int \frac{d^3p}{(2\pi)^3} \frac{f_{\text{eq}} - f}{\tau_{\text{rel}}} = \frac{n_{\text{eq}} - n}{\langle \tau_{\text{rel}} \rangle_c}, \quad (53)$$

which is a simple ansatz for the relaxation time [13]. The left-hand side of Eq. (53) is equal to $n(R_{23}/2 - R_{32}/3)$ if the explicit formulas of the collision terms and the definition of the collision rates are applied. We then obtain

$$\langle \tau_{\text{rel}} \rangle_c = \frac{1/\lambda_g - 1}{R_{23}/2 - R_{32}/3}, \quad (54)$$

where the gluon fugacity is $\lambda_g = n/n_{\text{eq}}$.

Assuming that the relaxation time is independent of the momentum, $\langle \tau_{\text{rel}} \rangle_k$ and $\langle \tau_{\text{rel}} \rangle_c$ become equal and one gets from Eq. (52)

$$\langle \tau_{\text{rel}} \rangle_k = \frac{1}{\lambda_g} \frac{1}{R_{22}^{\text{tr}} + R_{23}^{\text{tr}} + R_{32}^{\text{tr}}}. \quad (55)$$

In chemical equilibrium ($\lambda_g = 1$) the relaxation time is equal to the inverse of the total transport collision rate or the mean transport path. According to the relaxation time approximation the right-hand sides of Eqs. (54) and (55) should be equal. However, it is not clear.

Without assuming the relaxation time ansatz we can also calculate the $\langle\tau_{\text{rel}}\rangle_c$ and $\langle\tau_{\text{rel}}\rangle_k$ using Eqs. (54) and (52), because all the collision rates and the transport collision rates are known from numerical simulations. If the two “relaxation times” differ much, one can conclude that $\tau_{\text{rel}}(x, p)$ is strongly momentum dependent and cannot serve as a global quantity to determine the overall gluon thermalization time scale in ultrarelativistic heavy-ion collisions.

Before we calculate $\langle\tau_{\text{rel}}\rangle_c$ and $\langle\tau_{\text{rel}}\rangle_k$, we need the equilibrium particle density function $f_{\text{eq}}(x, p)$. Because we neglect quantum effects like gluon enhancement, $f_{\text{eq}}(x, p) = \nu e^{-E/T}$ at the center of the collision, where $\nu = 16$ is the degeneracy of gluons. The temperature T can be found using $\epsilon_{\text{eq}} = \epsilon$, which stems from energy conservation in sudden thermalization [9]. However, the current particle density function could have an exponential shape, $f = \lambda_g f_{\text{eq}}$, if the kinetic equilibration progressed quicker than chemical equilibration. In this case one obtains $n = \lambda_g n_{\text{eq}}$ as well as $\epsilon = \lambda_g \epsilon_{\text{eq}}$ and the temperature is then $T = \epsilon_{\text{eq}}/3n_{\text{eq}} = \epsilon/3n$. This temperature is larger (or smaller) than the previously defined temperature, if λ_g is smaller (or larger) than 1. The difference in these two local temperatures leads to the difference in ϵ_{eq} , n_{eq} , and λ_g . Letting S denote sudden thermalization and E thermalization that follows an exponential behavior, it is easy to verify that

$$\lambda_g^E = (\lambda_g^S)^4 = \frac{27\pi^2}{16} \frac{n^4}{\epsilon^3}, \quad (56)$$

where they differ by a power of 4. The time evolution of the gluon fugacities λ_g^S and λ_g^E obtained from BAMPS, including pQCD bremsstrahlung processes is shown in Fig. 15. Although the system of minijets is initially slightly oversaturated, it becomes undersaturated due to a short period of (quasi-)free streaming. The reason is obvious from Eq. (56), when n as well as ϵ decreases as $1/t$ in free streaming. The decrease of λ_g^E is roughly a factor of 4 stronger than that of λ_g^S . Whereas λ_g^E increases and relaxes to 1 later on, which indicates the ongoing chemical equilibration, $\lambda_g^S \approx 1$ throughout the entire expansion, which implies that the system is in chemical equilibrium. The difference between λ_g^S and λ_g^E can be understood according to Eq. (56), so $(\lambda_g^E - 1) \approx 4(\lambda_g^S - 1)$ for $|\lambda_g^S - 1| \ll 1$.

Physically, fugacity is a quantity that balances particle production and annihilation. Therefore, the ratio of the annihilation rate R_{32} to the production rate R_{23} can serve as a quantitative measure of fugacity, so, $2R_{32}/3R_{23}$ is shown in Fig. 15. $2R_{32}/3R_{23}$ agrees well with λ_g^E , which implies that λ_g^E is an appropriate choice for the fugacity in this example.

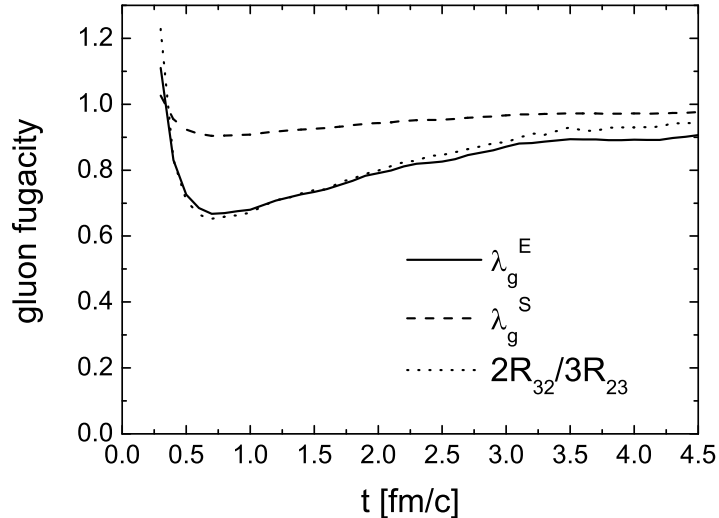


FIG. 15: Gluon fugacity. The solid, dashed, and dotted curve depict, respectively, λ_g^E , λ_g^S , and $2R_{32}/3R_{23}$ obtained from the simulation, including elastic and inelastic pQCD bremsstrahlung processes.

The exact momentum averaged “relaxation times” $\langle\tau_{\text{rel}}\rangle_k$ and $\langle\tau_{\text{rel}}\rangle_c$ according to Eqs. (52) and (54) are shown in Fig. 16 by various gluon fugacities. The mean transport path $1/(R_{22}^{\text{tr}} + R_{23}^{\text{tr}} + R_{32}^{\text{tr}})$ is also depicted for comparison. Except for $\langle\tau_{\text{rel}}\rangle_k$ with λ_g^S all “relaxation times” are considerably larger than the mean transport path. When comparing $\langle\tau_{\text{rel}}\rangle_k$ to $\langle\tau_{\text{rel}}\rangle_c$ with the same fugacities, one finds large differences, especially for λ_g^E , where both “relaxation times” deviate by a factor of 4 to 6. This implies that the relaxation time $\tau_{\text{rel}}(x, p)$ in Eq. (51) indeed has a strong dependence on the momentum. Therefore, the applicability of the $\tau_{\text{rel}}(x, p) \approx \tau_{\text{rel}}(x)$ in studying gluon thermalization in heavy-ion collisions is questionable.

VII. SUMMARY

Employing our recently developed parton cascade BAMPS and including inelastic pQCD bremsstrahlung processes we have introduced and calculated the transport rate of gluon drift and the transport collision rates of various scattering processes within relativistic kinetic theory. We try to explain the observed fast equilibration of gluons within BAMPS in theoretical terms.

We have shown that the derived transport rate of a certain process, $R_{\text{drift}}^{\text{tr}}$, R_{22}^{tr} , R_{23}^{tr} , or R_{32}^{tr} ,

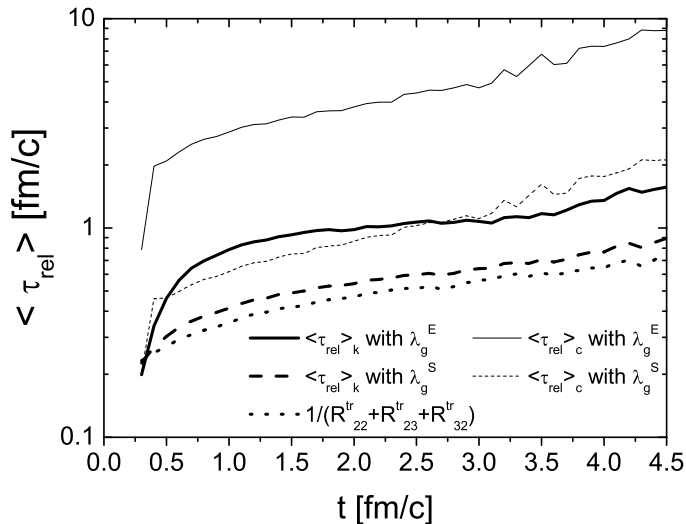


FIG. 16: Relaxation time. The thick (thin) solid curve depicts the momentum averaged “relaxation time” $\langle \tau_{\text{rel}} \rangle_k$ ($\langle \tau_{\text{rel}} \rangle_c$) using the fugacity λ_g^E . The thick (thin) dashed curve depicts $\langle \tau_{\text{rel}} \rangle_k$ ($\langle \tau_{\text{rel}} \rangle_c$) using the fugacity λ_g^S . The dotted curve shows again the mean transport path (see Fig. 10). Results are obtained from the simulation, including both elastic and inelastic pQCD-scattering processes.

determines exactly the contribution of the process to the defined momentum isotropization with $Q = \langle p_z^2/E^2 \rangle$ (or $Q = \langle |p_z|/E \rangle$). The total transport collision rate, $R_{22}^{\text{tr}} + R_{23}^{\text{tr}} + R_{32}^{\text{tr}}$, definitively describes momentum isotropization, whereas the change of gluon drift is a consequence of collision processes and $R_{\text{drift}}^{\text{tr}}$ is negative in an expanding system. The inverse of the total transport rate, $1/(R_{\text{drift}}^{\text{tr}} + R_{22}^{\text{tr}} + R_{23}^{\text{tr}} + R_{32}^{\text{tr}})$, gives the exact time scale of momentum isotropization θ_{rel} , and is about 1 fm/c from BAMPS for the gluon matter produced at RHIC. It is also shown that the calculated transport rates are independent on the definition of the degree of momentum isotropy Q .

The inclusion of quarks into BAMPS is straightforward, but it is not yet completed. In the presence of quarks the Debye screening mass will be slightly larger, which leads to a decrease in the cross sections for $gg \rightarrow gg$ and $gg \rightarrow ggg$ scatterings. This slightly slows thermalization. However, further kinetic processes like $q + g \leftrightarrow q + g$, $q + g \leftrightarrow q + g + g$ and $q + q \leftrightarrow q + q + g$ will speed up gluon thermalization. In addition, the effect may be small, because the initial quark density is tiny (30%) in comparison to the gluon density. Therefore, quark thermalization may be quite slow, but the study of it is still in progress.

We also derived the reduced transport collision rates related to the transport cross sections. They are only exact for the special case when the center-of-mass frame of individual collisions coincides with the laboratory frame where the medium is observed. The deviations from the exact transport collision rates stem from the effects of Lorentz boosts from the center-of-mass frame to the laboratory frame. The numerical results show that the reduced rates differ little from the exact ones for the evolution of gluons in relativistic heavy-ion collisions. Lorentz boosts do not seem to have a major effect on momentum isotropization. Nevertheless, the derivation of the transport collision rate helps to obtain the correct kinematical factors in the reduced rates summarized in Eqs. (46) and (47), which have been typically ignored in the literature. For instance, our analyses showed that a $2 \rightarrow N$ ($N > 2$) production process is about a factor of $(N-2)/2$ more efficient for momentum isotropization than its back-reaction or an elastic-scattering process.

Using the numerical results of the transport collision rates for the various scattering processes we have investigated the importance of including the pQCD bremsstrahlung processes in thermalization. The inclusion of the pQCD bremsstrahlung processes and their back reactions, as implemented in BAMPS, increases the efficiency for thermalization by a factor of 5. Overall kinetic equilibration and pressure buildup have a time scale of about 1 fm/c. The large efficiency stems partly from the increase in the particle number for the final state of $gg \rightarrow ggg$ collisions but mainly from the almost isotropic angular distribution in the bremsstrahlung process due to the effective implementation of LPM suppression, which still needs to be further developed.

Additionally, we have calculated the momentum averaged “relaxation times” with various gluon fugacities and they differ significantly from each other. This indicates a strong momentum dependence of the gluon relaxation time τ_{rel} in heavy-ion collisions. Thus, using the standard relaxation time approximation of full kinetic Boltzmann processes is questionable.

Acknowledgments

The authors thank B. Müller for the suggestion to analyze the thermalization time scale within the kinetic parton cascade BAMPS. We are also indebted to M. Gyulassy for enlightening discussions. The authors thank J. Noronha-Hostler and B. Schenke for the careful reading of the manuscript. C.G. thanks the Galileo Galilei Institute for Theoretical Physics

for its hospitality and the INFN for partial support during the completion of this work.

APPENDIX A: DEGREE OF MOMENTUM ISOTROPY IN THE CENTRAL REGION

The central region is described by a cylinder with a radius of $r_b = 1.5$ fm and a longitudinal extension of $2Z_b$. The longitudinal boundary $Z_b = (\tanh \eta_b) t$ with $\eta_b = 0.2$ increases linearly with time. Within the central region the degree of momentum isotropy is defined by

$$\begin{aligned} Q(t) &:= \frac{1}{n} \int \frac{d^3p}{(2\pi)^3} \frac{p_z^2}{E^2} \frac{1}{V} \int_0^{r_b} dr r \int_0^{2\pi} d\phi \int_{-Z_b}^{Z_b} dz f(\vec{x}, t, p) \\ &= \frac{1}{n} \int \frac{d^3p}{(2\pi)^3} \frac{p_z^2}{E^2} \frac{2}{V} \int_0^{r_b} dr r \int_0^{2\pi} d\phi \int_0^{Z_b} dz f(\vec{x}, t, p), \end{aligned} \quad (\text{A1})$$

where

$$n(t) = \int \frac{d^3p}{(2\pi)^3} \frac{2}{V} \int_0^{r_b} dr r \int_0^{2\pi} d\phi \int_0^{Z_b} dz f(\vec{x}, t, p). \quad (\text{A2})$$

$V = 2\pi r_b^2 Z_b$ is the volume of the central region. The second equation in Eq. (A1) arises because of the symmetry of $f(\vec{x}, t, p)$ under the $\vec{x} \rightarrow -\vec{x}$ exchange. In the limit $r_b \rightarrow 0$ and $\eta_b \rightarrow 0$ one has

$$\frac{1}{V} \int_0^{r_b} dr r \int_0^{2\pi} d\phi \int_{-Z_b}^{Z_b} dz f(\vec{x}, t, p) \rightarrow f(\vec{x}, t, p)|_{\vec{x}=0}, \quad (\text{A3})$$

which is the definition of the degree of the local momentum isotropy in this limit [see Eq. (10) in Sec. V]. The transport rates in this limit were already given in Sec. V.

Taking the time derivative of $Q(t)$ yields

$$\begin{aligned} \dot{Q}(t) &= \frac{1}{n} \int \frac{d^3p}{(2\pi)^3} \frac{p_z^2}{E^2} \frac{2}{V} \int_0^{r_b} dr r \int_0^{2\pi} d\phi \left[\int_0^{Z_b} dz \frac{\partial f}{\partial t} + \tanh \eta_b f(\vec{x}_\perp, Z_b, t, p) \right] \\ &\quad - Q(t) \frac{1}{n} \int \frac{d^3p}{(2\pi)^3} \frac{2}{V} \int_0^{r_b} dr r \int_0^{2\pi} d\phi \left[\int_0^{Z_b} dz \frac{\partial f}{\partial t} + \tanh \eta_b f(\vec{x}_\perp, Z_b, t, p) \right]. \end{aligned} \quad (\text{A4})$$

The second term in the brackets comes from the time derivative of the boundary Z_b and can be rewritten as

$$\tanh \eta_b f(\vec{x}_\perp, Z_b, t, p) = \int_0^{Z_b} dz \frac{\tanh \eta_b}{Z_b} f(\vec{x}_\perp, Z_b, t, p) = \int_0^{Z_b} dz \frac{1}{t} f(\vec{x}_\perp, Z_b, t, p). \quad (\text{A5})$$

The Taylor expansion of $f(\vec{x}_\perp, Z_b, t, p)$ at \vec{x} to the first order yields

$$f(\vec{x}_\perp, Z_b, t, p) \simeq f(\vec{x}, t, p) + \frac{\partial f(\vec{x}, t, p)}{\partial z} (Z_b - z) \quad (\text{A6})$$

and we then obtain

$$\begin{aligned} \dot{Q}(t) \simeq & \frac{1}{n} \int \frac{d^3p}{(2\pi)^3} \frac{p_z^2}{E^2} \frac{2}{V} \int_0^{r_b} dr r \int_0^{2\pi} d\phi \int_0^{Z_b} dz \left[\frac{\partial f}{\partial t} + \frac{(Z_b - z)}{t} \frac{\partial f}{\partial z} \right] \\ & - Q(t) \frac{1}{n} \int \frac{d^3p}{(2\pi)^3} \frac{2}{V} \int_0^{r_b} dr r \int_0^{2\pi} d\phi \int_0^{Z_b} dz \left[\frac{\partial f}{\partial t} + \frac{(Z_b - z)}{t} \frac{\partial f}{\partial z} \right]. \end{aligned} \quad (\text{A7})$$

The 0th-order contributions in Eq. (A4) cancel due to the definition of $Q(t)$. $(Z_b - z)/t$ expresses the relative velocity of the boundary slice at Z_b to the slice at z where particles are sitting. The second term in the brackets in Eq. (A7) appears due to the increasing longitudinal boundary of the central region, and it becomes smaller when $Z_b \rightarrow 0$ (or $\eta_b \rightarrow 0$). According to the Boltzmann equation (13) the expression in the brackets can be written as

$$\frac{\partial f}{\partial t} + \frac{(Z_b - z)}{t} \frac{\partial f}{\partial z} = -\frac{p_x}{E} \frac{\partial f}{\partial x} - \frac{p_y}{E} \frac{\partial f}{\partial y} - \left(\frac{p_z}{E} - \frac{Z_b - z}{t} \right) \frac{\partial f}{\partial z} + C_{22} + C_{23} + C_{32}. \quad (\text{A8})$$

The term $p_z/E - (Z_b - z)/t$ implies that only particles with longitudinal velocity p_z/E larger than the relative velocity of the boundary slice $(Z_b - z)/t$ can drift out of the central region. This will be taken into account when calculating the transport rate of particle drift within the central region. The evaluations of the transport collision rates R_{22}^{tr} , R_{23}^{tr} , and R_{32}^{tr} are more straightforward. One only needs to replace the expressions derived in the limit $r_b \rightarrow 0$ and $\eta_b \rightarrow 0$, which are already given in Sec. V, by

$$R_i^{\text{tr}} \rightarrow \frac{1}{V} \int_0^{r_b} dr r \int_0^{2\pi} d\phi \int_{-Z_b}^{Z_b} dz R_i^{\text{tr}}, \quad (\text{A9})$$

where $i = 22, 23, \text{ or } 32$.

-
- [1] M. Gyulassy and L. McLerran, Nucl. Phys. A **750**, 30 (2005).
 - [2] P. Huovinen, P.F. Kolb, U.W. Heinz, P.V. Ruuskanen, and S.A. Voloshin, Phys. Lett. B **503**, 58 (2001).
 - [3] S.S. Adler *et al.* (PHENIX Collaboration), Phys. Rev. Lett. **91**, 182301 (2003).
 - [4] J. Adams *et al.* (STAR Collaboration), Phys. Rev. Lett. **92**, 052302 (2004).
 - [5] Z. Xu and C. Greiner, Phys. Rev. C **71**, 064901 (2005).
 - [6] Z. Xu and C. Greiner, Nucl. Phys. A **774**, 787 (2006).
 - [7] P. Danielewicz and M. Gyulassy, Phys. Rev. D **31**, 53 (1985).

- [8] M.H. Thoma, Phys. Rev. D **49**, 451 (1994).
- [9] G. Baym, Phys. Lett. B **138**, 18 (1984).
- [10] A. Hosoya and K. Kajantie, Nucl. Phys. B **250**, 666 (1985).
- [11] S. Gavin, Nucl. Phys. B **351**, 561 (1991).
- [12] H. Heiselberg and Xin-Nian Wang, Phys. Rev. C **53**, 1892 (1996).
- [13] S.M.H. Wong, Nucl. Phys. A **607**, 442 (1996).
- [14] A. Dumitru and M. Gyulassy, Phys. Lett. B **494**, 215 (2000).
- [15] J. Serreau and D. Schiff, J. High Energy Phys. **0111**, 039 (2001).
- [16] P. Danielewicz and G.F. Bertsch, Nucl. Phys. A **533**, 712 (1991).
- [17] A. Lang, H. Babovsky, W. Cassing, U. Mosel, H.G. Reusch, and K. Weber, J. Comp. Phys. **106**, 391 (1993).
- [18] W. Cassing, Nucl. Phys. A **700**, 618 (2002).
- [19] D. Molnar, Nucl. Phys. A **661**, 205 (1999).
- [20] J.F. Gunion and G. Bertsch, Phys. Rev. D **25**, 746 (1982).
- [21] T.S. Biro, E. van Doorn, B. Müller, M.H. Thoma, and X.-N. Wang, Phys. Rev. C **48**, 1275 (1993).
- [22] T.S. Biro, B. Müller, and X.-N. Wang, Phys. Lett. B **283**, 171 (1992).
- [23] S. Mrówczyński, Phys. Lett. B **314**, 118 (1993); Phys. Rev. C **49**, 2191 (1994); Phys. Lett. B **393**, 26 (1997); Acta. Phys. Pol. B **37**, 427 (2006).
- [24] P. Arnold, J. Lenaghan, and G.D. Moore, J. High Energy Phys. **0308**, 002 (2003).
- [25] P. Arnold, J. Lenaghan, G.D. Moore, and L.G. Yaffe, Phys. Rev. Lett. **94**, 072302 (2005).
- [26] A. Rebhan, P. Romatschke, and M. Strickland, Phys. Rev. Lett. **94**, 102303 (2005).
- [27] A. Dumitru and Y. Nara, Phys. Lett. B **621**, 89 (2005).
- [28] B. Schenke, M. Strickland, C. Greiner, and M.H. Thoma, Phys. Rev. D **73**, 125004 (2006).
- [29] K.J. Eskola, K. Kajantie, and J. Lindfors, Nucl. Phys. B **323**, 37 (1989).
- [30] X.N. Wang and M. Gyulassy, Phys. Rev. D **44**, 3501 (1991).
- [31] K.J. Eskola and X.N. Wang, Phys. Rev. D **49**, 1284 (1994).
- [32] L.D. McLerran and R. Venugopalan, Phys. Rev. D **49**, 2233 (1994); *ibid.* **49**, 3352 (1994).
- [33] J. Adams *et al.* (STAR Collaboration), Phys. Rev. C **70**, 054907 (2004).
- [34] J.D. Bjorken, Phys. Rev. D **27**, 140 (1983).
- [35] H. Satz and D.K. Srivastava, Phys. Lett. B **475**, 225 (2000).

[36] S.A. Bass, B. Müller, and D.K. Srivastava, Phys. Lett. B **551**, 277 (2003).